Mechanistic Understanding of Aging Behaviors of Critical-Material-Free $Li_4Ti_5O_{12}$// $LiNi_{0.9}Mn_{0.1}O_2$ Cells with Fluorinated Carbonate-Based Electrolytes for Safe Energy Storage with Ultra-Long Life Span

Yicheng Zhang, Glenn Teeter, Nikita S. Dutta, Sarah Frisco, Sang-Don Han*

Materials, Chemical, and Computational Science Directorate, National Renewable Energy Laboratory, 15013 Denver West Parkway, Golden, CO 80401, USA
E-mail: sang-don.han@nrel.gov

Keywords: behind-the-meter-storage, no cobalt cathodes, lithium titanate, fluorinated carbonate, electrode-electrolyte interphase.

Pursuant to the DOE Public Access Plan, this document represents the authors' peer-reviewed, accepted manuscript. The published version of the article is available from the relevant publisher.

Graphical abstract

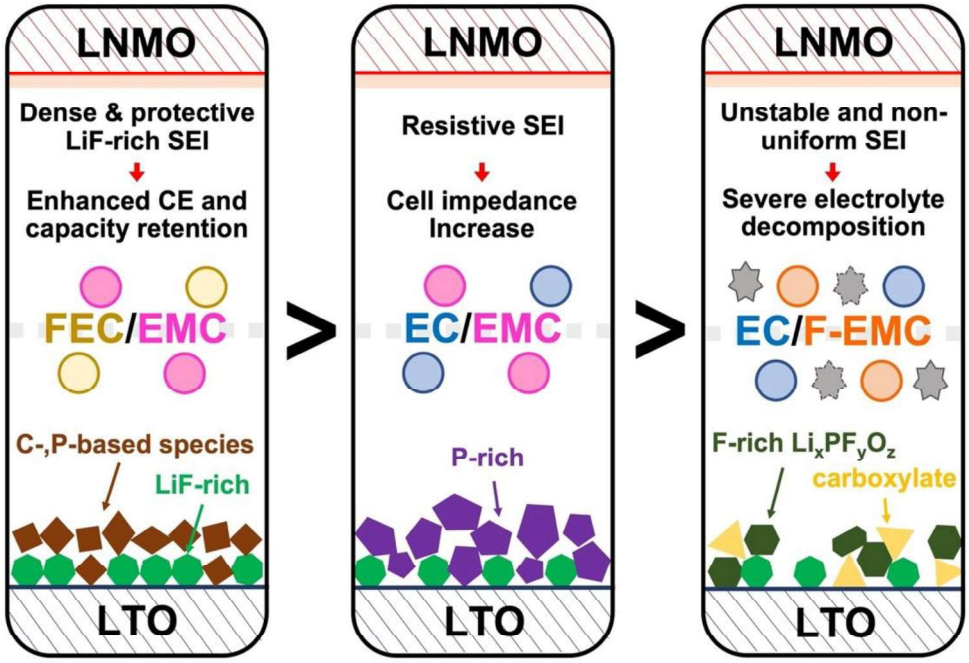

Pursuant to the DOE Public Access Plan, this document represents the authors' peer-reviewed, accepted manuscript.
The published version of the article is available from the relevant publisher.

Abstract

Behind-the-meter storage (BTMS) systems—a viable method to minimize potential risk of blackout events and stabilize the grid—require a different type of cost-effective energy storage with excellent safety, ultra-long (>20 years) cycle life and reasonable energy density compared that of electric vehicles. To increase the energy density and reduce the cost of a long-term cyclable lithium-titanate-based cell, it is required to employ a critical-material-free high voltage cathode and an electrolyte with good electrochemical and transport properties. Here, the long-term electrochemical performance and behaviors of selected critical-material-free $Li_4Ti_5O_{12}$ (LTO)//$LiNi_{0.9}Mn_{0.1}O_2$ (LNMO) full cells for BTMS applications are evaluated and analyzed in the optimized voltage range of 1.4-2.7 V at 45°C with different fluorinated carbonate-based electrolytes. The fluoroethylene carbonate (FEC)-based electrolyte cell shows the highest capacity retention of 57.9% and Coulombic efficiency (CE) of 99.96% after 1000 cycles, potentially attributed to a dense, homogenous and less resistive LiF-rich solid-electrolyte interphase (SEI) layer formed on the surface of LTO that may mitigate electrolyte decomposition and maintain relatively low cell impedance during cycling. The 3,3,3-fluoroethylmethyl carbonate (F-EMC)-based electrolyte cell, however, presents the worst performance with lower capacity and a sharp decrease of CE, due to unstable and non-uniform SEI formation and continuous oxidative electrolyte decomposition. This mechanistic understanding of cell aging behaviors and failure mechanisms with detailed analysis of surface chemistry and electrode morphology can guide design of new electrode chemistries and electrolyte formulations for the development of BTMS batteries.

Pursuant to the DOE Public Access Plan, this document represents the authors' peer-reviewed, accepted manuscript.
The published version of the article is available from the relevant publisher.

1. Introduction

An energy storage system (ESS) can add value to the power system by improving its flexibility and stability. A behind-the-meter storage (BTMS) system is a stationary ESS connected to the distribution system on the customer's side of the utility's service meter.[1] Generally, BTMS system are integrated with energy production (e.g., solar photovoltaics or wind turbines) and energy utilization (e.g., electrical vehicle supply equipment or buildings), in order to provide optimized energy storage at minimal cost. Thus, for BTMS—a relatively less volume and weight sensitive system—applications, development of cost-effective energy storage with excellent safety and ultra-long (>20 years) cycle life is preferable to one with higher energy density. Among energy storage options, lithium-ion batteries (LiBs) are an attractive technology due to their high specific capacity and energy density, relatively good cycling stability, and significant recent declines in cost.[2-4] Critical-material-free LiB chemistries are even more desirable, considering the high price and limited abundance of critical materials such as cobalt (Co).[5] Most importantly, LiBs based on new chemistries are required for BTMS applications. For example, graphite//$LiFePO_4$ is one of popular cell chemistries for electric vehicle applications due to its cost-effectiveness and relatively stable cyclability,[6-8] but it is not a satisfactory battery chemistry for BTMS application in terms of cycle life and safety.

To achieve ultra-long cycle life and safety with LiBs, lithium titanate ($Li_4Ti_5O_{12}$, LTO) is a promising anode candidate due to its well-known excellent long-term cycling stability.[9,10] Specifically, LTO is known as a "zero-strain" material with negligible volume changes during lithium (Li) ion intercalation/de-intercalation, resulting in good capacity retention upon cycling.[11] In addition, LTO shows flat charge and discharge plateaus at about 1.5 V *vs*. Li/Li^+ with a reversible capacity of above 160 mAh g^{-1};[11-13] this high working voltage can prevent Li plating and dendritic growth, which improves battery cyclability and safety.[14]

On the cathode side, materials with little or no Co have attracted attention because of the limited abundance and high price of Co. In the 1990s and 2000s, $LiNi_{1-x}Mn_xO_2$ ($0<x<1$) have been

Pursuant to the DOE Public Access Plan, this document represents the authors' peer-reviewed, accepted manuscript.
The published version of the article is available from the relevant publisher.

extensively studied.[15-18] Specifically, $LiNi_{0.5}Mn_{0.5}O_2$ drew attention due to its relatively high capacity and better thermal stability.[16-18] However, it was found that the cathode materials with higher Ni content have higher capacities and voltages.[19] Among recently developed Ni-rich cathode materials, $LiNi_{0.9}Mn_{0.1}O_2$ (LNMO) is a good candidate for BTMS applications due to its high capacity, high operating voltage and relatively low price.[20-23] High-Ni layered oxides including LNMO, however, suffer from limited cycling stability due to structural instabilities (e.g., irreversible phase transitions), mechanical failure (e.g., crack formations) and unstable cathode-electrolyte interphase (CEI) formation at high voltages.[21-25] During charging, highly active Ni^{4+} ions on the cathode surface may react with electrolytes leading to oxidative electrolyte decomposition, surface structure deterioration, Ni dissolution, cross-talk and oxygen release with potential safety issues.[24,26] To suppress those side reactions, electrode surface modifications, such as surface coating with Al_2O_3, TiO_2, or $LiPO_3$, have been employed for high-Ni layered oxides and demonstrated improvements in cell performance.[27-29]

In addition to electrode surface modifications, new electrolyte formulation with fluorinated solvents or sulfonamide-based solvents and/or additive(s) is a promising strategy to form a protective and stable CEI layer on high-Ni cathodes to mitigate parasitic interfacial reactions.[30-33] In particular, fluorinated solvents, such as fluorinated cyclic carbonates (e.g., fluoroethylene carbonate (FEC) and trifluoropropylene carbonate (TFPC)), fluorinated linear carbonates (e.g., 3,3,3-fluoroethylmethyl carbonate (F-EMC) and di-(2,2,2-trifluoroethyl) carbonate (F-DEC)) and fluorinated ethers (e.g., 1,1,2,2-tetrafluoroethyl-2′,2′,2′-trifluoroethyl ether (HFE) and 1,1,2,2-tetrafluoroethyl-2,2,3,3-tetrafluoropropyl ether (F-EPE)), have been studied extensively as potential next-generation electrolytes generally due to their good oxidative stability, non-flammability and stable electrode-electrolyte interphase formation.[30-32,34-41] Among these, FEC is well known for promoting the formation of a robust LiF-rich solid-electrolyte interphase (SEI) on variety of anodes including graphite,[39] silicon,[34,42] Li metal,[31] and LTO,[43] while F-EMC based electrolytes have been found to form stable F-rich SEI and

Pursuant to the DOE Public Access Plan, this document represents the authors' peer-reviewed, accepted manuscript.
The published version of the article is available from the relevant publisher.

CEI layers on Li metal anodes and Ni-rich layered cathodes, respectively.[30,37,40] Compared to other anode protection methods including surface coating,[44-47] new electrolyte formulation is more facile and cost-effective approach and also easy to scale up.

Our previous work[10] has demonstrated that Ni-rich cathodes with high reversible capacities are required to increase the energy density of LTO anode-based cells. Ethylene carbonate (EC)-based electrolytes with a secondary solvent that is electrochemically stable and has good transport properties (e.g., low viscosity and high ionic conductivity) are also necessary to utilize thick electrodes and enhance energy density of the cells. In this paper, therefore, we analyze the electrochemical behavior and performance of $Li_4Ti_5O_{12}$//$LiNi_{0.9}Mn_{0.1}O_2$ full cells with $LiPF_6$-based electrolytes with FEC or F-EMC as co-solvents and investigate the surface morphology and chemistry changes of both electrodes. The cells demonstrated high initial discharge energy density of 447 Wh kg^{-1} (at 1C) that is comparable with other reported 2-3 V Li/Na-ion full cells.[48-50] Detailed electrochemical analysis and diagnostics and comprehensive post-mortem characterization provide a fundamental and mechanistic understanding of cell aging behaviors and failure mechanisms to guide design of new electrode chemistries and electrolyte formulations for a BTMS energy storage.

2. Results and Discussion

2.1. Electrolyte Properties

Ionic conductivities of three selected electrolytes—1.2 M lithium hexafluorophosphate ($LiPF_6$) in ethylene carbonate (EC):ethyl methyl carbonate (EMC) (3:7 wt.%) (Gen2 as a reference), 1.0 M $LiPF_6$ in FEC:EMC (3:7 wt.%) (FEC/EMC) and 1.0 M $LiPF_6$ in EC:F-EMC (7:3 wt.%) (EC/F-EMC)—were measured in 10°C steps from 25°C to 55°C with the samples equilibrated at each temperature in the aluminum heating block for more than 20 min prior to the measurements (Fig. 1a). For each electrolyte, at least two measurements were made with a fresh sample used after each analysis. Compared with the reference Gen2 electrolyte, both fluorinated

Pursuant to the DOE Public Access Plan, this document represents the authors' peer-reviewed, accepted manuscript.
The published version of the article is available from the relevant publisher.

solvent-based electrolytes showed comparable ionic conductivities. Specifically, at 45°C—standard cell cycling temperature to improve the cell kinetics by facilitating Li^+ ion diffusion in the electrodes and increasing ionic conductivity of the electrolyte for higher energy density with thicker electrodes and better rate capability—the conductivities followed: Gen2 > FEC/EMC > EC/F-EMC.

Linear sweep voltammetry (LSV) measurements were performed for Gen2, FEC/EMC and EC/F-EMC electrolytes at both 25°C (room temperature, RT) and 45°C to evaluate their electrochemical stability (Fig. 1b). Each scan started at open circuit voltage (OCV) and stopped at 5.0 V (*vs*. Li^+/Li^0, hereafter) with a scan rate of 25 mVs^{-1}. At RT, Gen2 and EC/F-EMC electrolytes showed negligible redox reactions below 4.5 V, whereas FEC/EMC electrolyte displayed oxidative reactions at above 4.2 V with several anodic peaks between 4.2 and 5.0 V—interestingly demonstrating that one fluorinated solvent (FEC) based electrolyte had lower electrochemical stability than Gen2. On the other hand, at 45°C, all Gen2, FEC/EMC and EC/F-EMC electrolytes showed narrower electrochemical windows up to approximately 4.2, 4.0 and 3.2 V, respectively. The current curves of all electrolytes at 45°C showed similar shapes compared to those at RT, except for additional broad oxidation peak(s) starting at around 3.6 V for the EC/F-EMC electrolyte. In particular, up to 4.5 V—the upper cut-off voltage (UCV) for formation cycles (*vs*. 4.2 V UCV for the aging cycles) in the electrochemical tests—both Gen2 and FEC/EMC electrolytes showed relatively much fewer oxidation reactions, while EC/F-EMC electrolyte had apparent oxidation reaction(s) starting at about 3.6 V possibly due to its higher content (70%) of EC, which has relatively poor oxidative stability especially at high temperature (45°C).[51] It is noteworthy that even small chemical changes in the solvents (Fig. 1c) can change the electrolyte properties (e.g., ionic conductivity and electrochemical stability) at varying temperatures that directly influence battery performance, lifetime, and safety.

Pursuant to the DOE Public Access Plan, this document represents the authors' peer-reviewed, accepted manuscript.
The published version of the article is available from the relevant publisher.

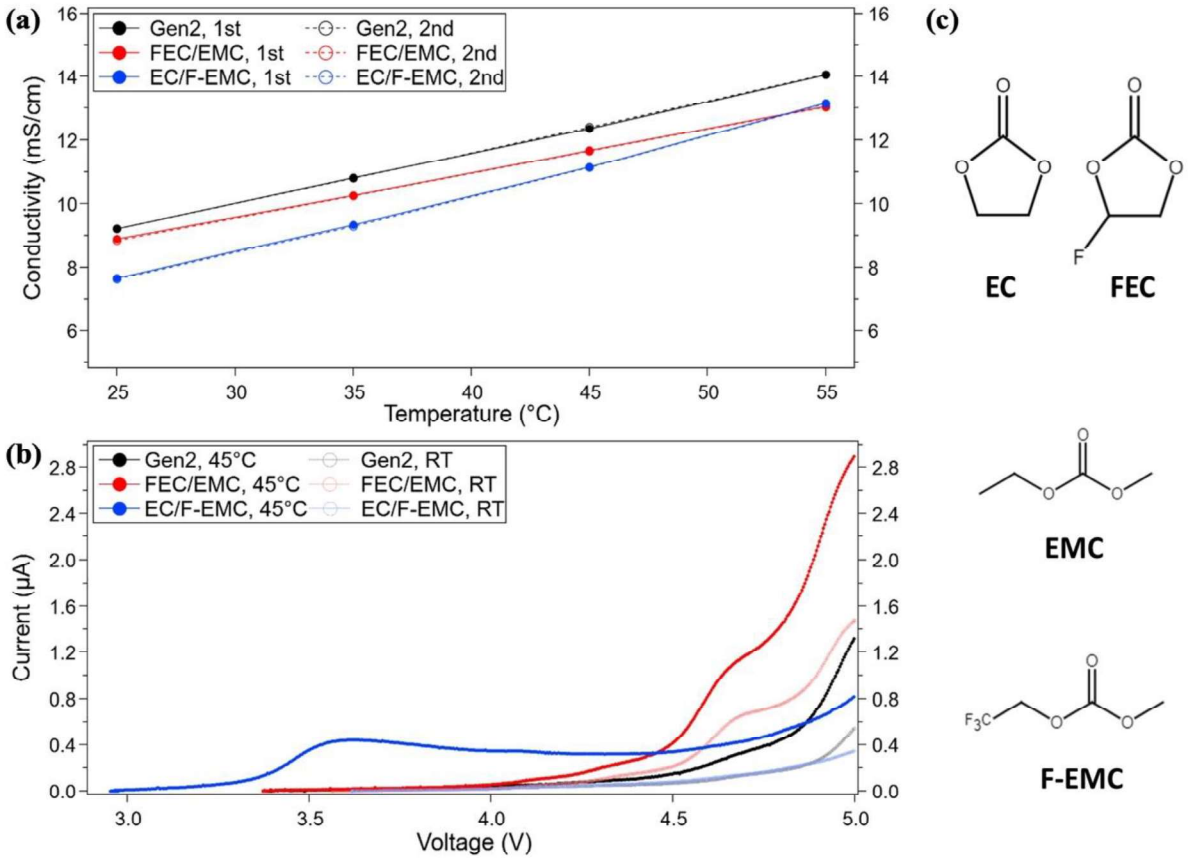

Figure 1. (a) Ionic conductivities of Gen2, FEC/EMC and EC/F-EMC electrolytes with varying temperatures. (b) LSVs of Gen2, FEC/EMC and EC/F-EMC electrolytes at 25°C and 45°C (the scan rate was 25 mV s^{-1}). (c) Chemical structures of EC, FEC, EMC and F-EMC solvents.

2.2. Electrochemical Behaviors and Cycling Performance (at 45°C)

Formation and aging cycles. Figs. 2a and 2b show the specific capacity *vs*. voltage profiles and corresponding differential capacity (dQ/dV) plot for the 1st formation cycle of the LNMO//LTO full cells with the three electrolytes. In the first cycle, cells with Gen2, FEC/EMC and EC/F-EMC electrolytes showed discharge capacities of 231.0, 223.7 and 218.6 mAh g^{-1} and Coulombic efficiencies (CEs) of 93.3, 88.9 and 90.5%, respectively. All dQ/dV plots displayed three typical high-Ni layered oxides redox peaks corresponding to hexagonal (H1) to monoclinic (M) to hexagonal (H2) to hexagonal (H3) phase transitions, regardless of different electrolytes (Fig. 2b).[20] During charging up to 3.0 V in Fig. 2a, the FEC/EMC electrolyte cell showed higher capacity compared to the Gen2 electrolyte cell, possibly originating from electrolyte decomposition at high voltages due to relatively lower electrochemical stability (Fig.

Pursuant to the DOE Public Access Plan, this document represents the authors' peer-reviewed, accepted manuscript.
The published version of the article is available from the relevant publisher.

1b). The EC/F-EMC electrolyte cell showed the lowest capacity among 3 cells, probably due to having the lowest conductivity at 45°C (Fig. 1a).

The high temperature cycling performances of each cell with different electrolytes are shown in Fig. 2c. The Gen2 electrolyte cell represents the highest reversible capacities for both formation and aging cycles up to about 650 cycles. Specifically, the capacity retention of aging cycles (1C) is better than that of FEC/EMC and EC/F-EMC electrolyte cells up to around 400 cycles, but the capacity curve crosses that of FEC/EMC electrolyte cell around 650 cycles due to a gradual increase in capacity fade rate. The capacity differences at C/10 *vs*. 1C in each 50-cycle term is relatively large and gets larger upon cycling, especially after 400 cycles. For example, the capacity difference between the 953rd cycle (C/10) and 955th cycle (1C) is 30.6 mAhg^{-1}, which is as about twice high as that of the 3rd cycle (C/10) and 5th cycle (16.1 mAhg^{-1}). The increasing capacity difference between C/10 and 1C rates indicates growing cell impedance upon cycling. In Fig. S1 (Supporting Information), the Gen2 electrolyte cell shows longer constant voltage (CV) hold time compared with the FEC/EMC electrolyte cell indicating additional possible side reactions, such as electrolyte decomposition, formation of unstable passivation layers on the electrode surfaces and surface phase transitions of the active materials, which may result in cell polarization, impedance increases and subsequent capacity fading.

Pursuant to the DOE Public Access Plan, this document represents the authors' peer-reviewed, accepted manuscript.
The published version of the article is available from the relevant publisher.

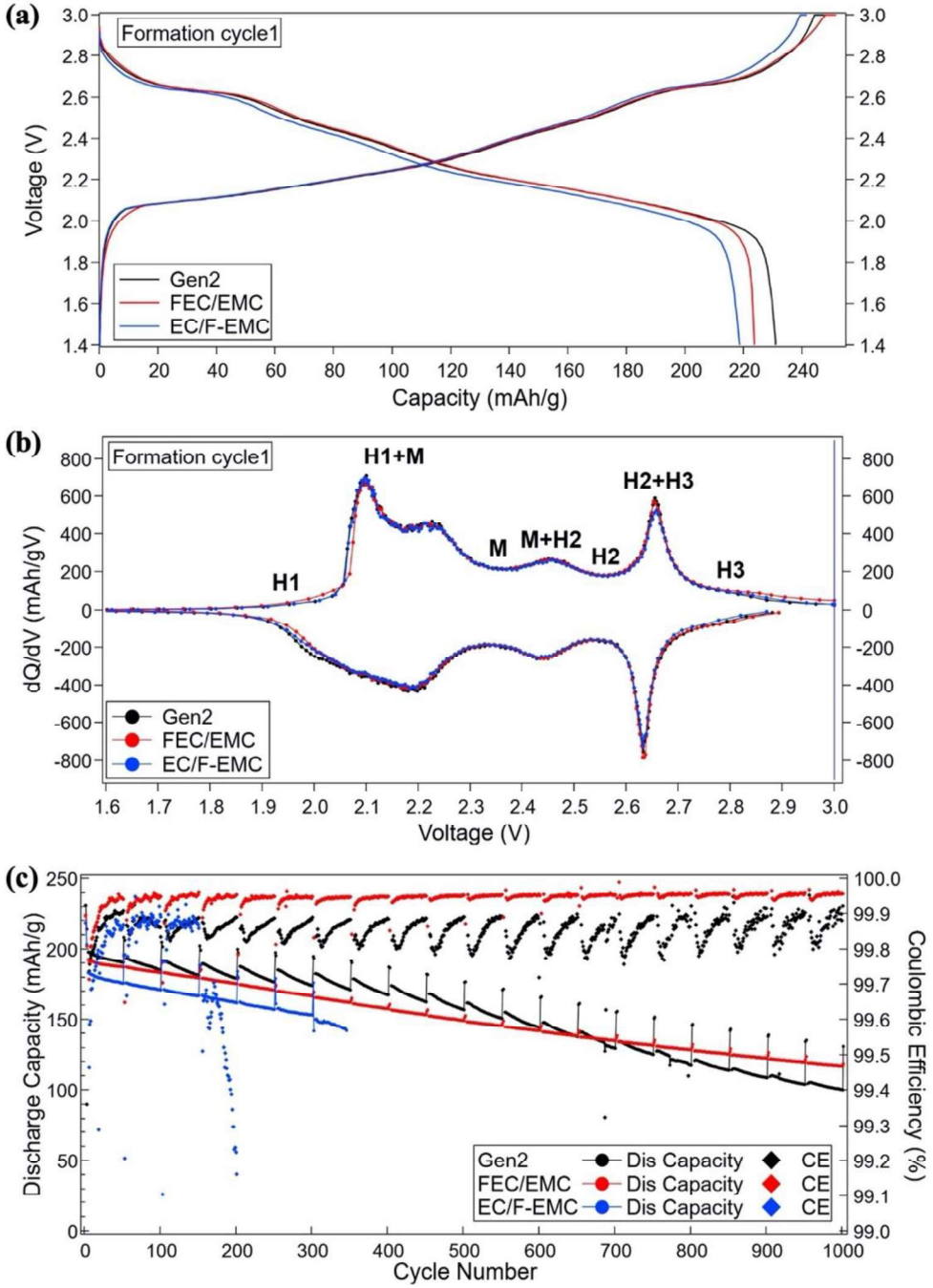

Figure 2. Electrochemical behaviors of LNMO//LTO full cells with three different electrolytes: (a) specific capacity *vs*. voltage profiles (in the voltage range of 1.4 – 3.0 V at C/10 (1C = 231 mA g^{-1}) with voltage hold at the end of charging until the applied current ≤ C/30) and (b) corresponding dQ/dV plots for the 1st formation cycle. (c) High temperature (45°C) cycling performance of LNMO//LTO full cells with three different electrolytes at C/10 for the 2 formation cycles in the voltage range of 1.4 – 3.0 V and 1C for the subsequent aging cycles in the voltage range of 1.4 – 2.7 V with voltage hold at the end of charging until the applied current ≤ C/30.

In the dQ/dV plots (Fig. 3a), all redox peaks of the Gen2 electrolyte cell decrease to similar extents indicating gradual impedance growth and loss of active material and/or lithium

Pursuant to the DOE Public Access Plan, this document represents the authors' peer-reviewed, accepted manuscript. The published version of the article is available from the relevant publisher.

inventory during cycling. Specifically, the H2-H3 phase transition is partially utilized as the polarization increases with cycles, and thus the corresponding peak diminishes more compared to other redox peaks. It is worth noting that the H2-H3 redox peak shifts to higher voltages, so it may take more time to extract lithium during the H2 → H3 phase transition during a voltage hold step (2.7 V) at the end of each charging (Fig. S1). The accumulated CE from the 3rd cycle to the 953rd cycle of the Gen2 electrolyte cell is 41.51%, whereas the percentage of discharge capacity retained in the 953rd cycle with respect to the 3rd cycle is 63.21%. The large difference between those two values suggests that the relatively low CE (~ 99.90%) of the Gen2 electrolyte cell originates from Li trapping in the anode and other Li consuming side reactions (e.g., solid-electrolyte interphase (SEI) formation and evolution) during discharging. The large amount of capacity gained by adding a voltage hold step at the end of the last 1C discharge cycle in every 50 cycles confirms the Li trapping behaviors (Fig. 2c).

Pursuant to the DOE Public Access Plan, this document represents the authors' peer-reviewed, accepted manuscript.
The published version of the article is available from the relevant publisher.

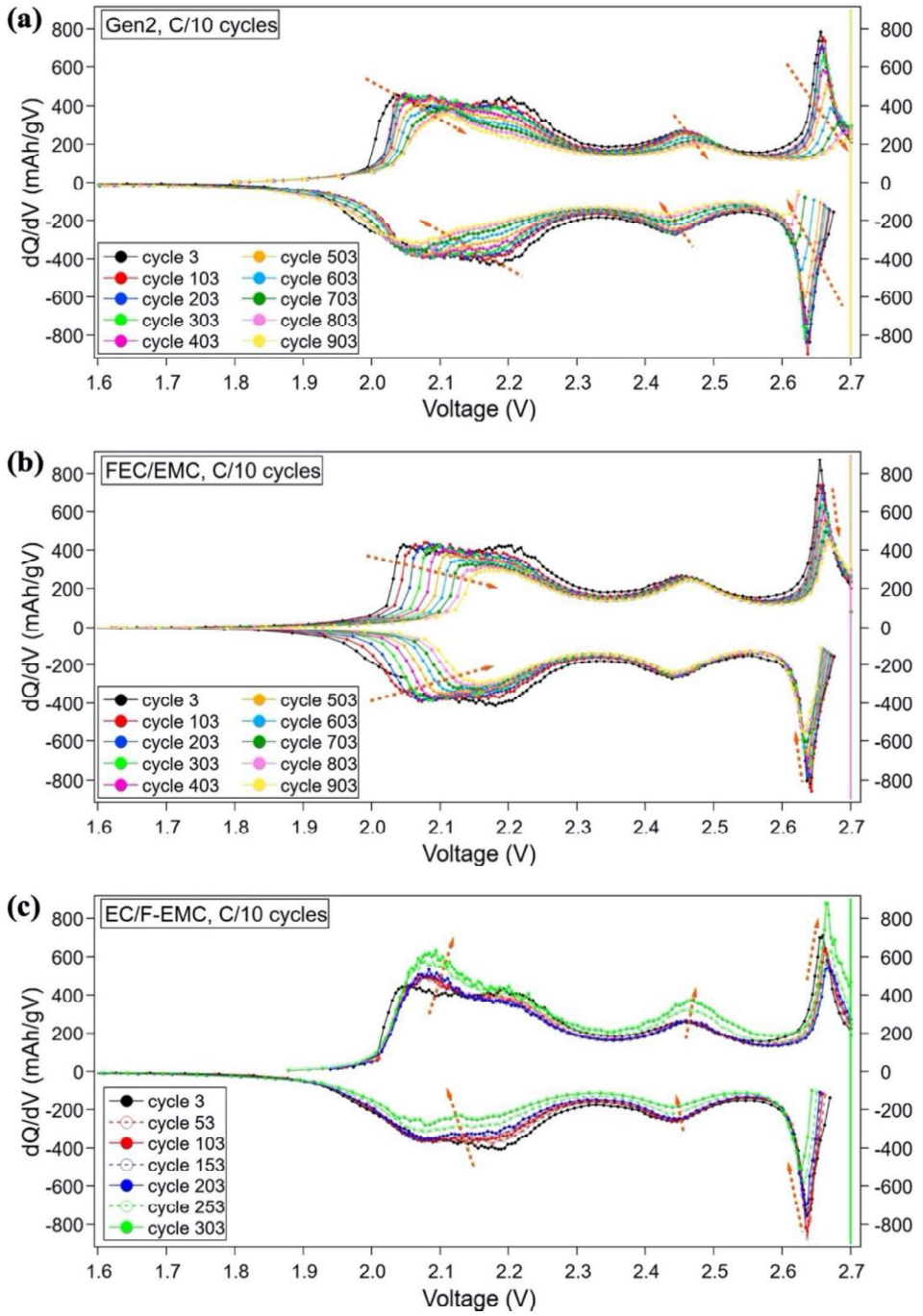

Figure 3. dQ/dV curves of (a) Gen2, (b) FEC/EMC and (c) EC/F-EMC electrolyte cells for C/10 aging cycles.

On the other hand, the FEC/EMC electrolyte cell displays a lower initial capacity compared to that of the Gen2 electrolyte cell, but a relatively consistent and slower capacity fade rate (negligible "slope change" in the capacity curve) is observed due to the formation of relatively thin, protective SEI layers (evidenced by post-mortem analyses) and less polarization (Fig. S2)

Pursuant to the DOE Public Access Plan, this document represents the authors' peer-reviewed, accepted manuscript.
The published version of the article is available from the relevant publisher.

by using fluorinated carbonate solvents. The difference between the C/10 capacity and 1C capacity is relatively small and becomes smaller upon cycling: the capacity differences are 9.3 $mAhg^{-1}$ for the 5^{th} cycle and 4.7 $mAhg^{-1}$ for the 955^{th} cycle, respectively. In addition, the CE stabilizes at a relatively high value of about 99.95%, suggesting the cell has relatively good kinetics. The remaining capacity fade, however, may originate from continuous loss of lithium inventory and/or active materials, considering that the H1-M redox peak decreases much more than the other two redox peaks (M-H2 and H2-H3) as shown in Fig. 3b. Here, the accumulated CE from the 3^{rd} cycle to the 953^{rd} cycle is 57.41%, and the discharge capacity retention percentage is 61.25%. The small difference between these values suggests relatively less Li trapping in the anode of the FEC/EMC cell compared to that of the Gen2 electrolyte cell.

In the case of EC/F-EMC electrolyte cell, it displays the lowest reversible capacity and poor capacity retention with a drastic CE drop after around 150 cycles (Fig. 2c). The continuous growth of oxidation peaks at high voltages after 150 cycles in the dQ/dV plot (Fig. 3c) may be correlated with the formation of unstable electrode-electrolyte interphase (EEI) layers and severe electrolyte decomposition because of relatively worse electrochemical stability (Fig. 1b) during charging. The large difference between C/10 and 1C capacities indicates poor kinetics in the cell; the relatively low conductivity of EC/F-EMC electrolyte (Fig. 1a) could be one reason. Overall, the EC/F-EMC electrolyte cell does not show desirable electrochemical performance in any aspect.

Areal specific impedance (ASI) and kinetic limitation. In Fig. S3 the EC/F-EMC electrolyte cell has the highest ASI for the 1^{st} aging cycle, especially in the low-voltage range (< 2.1 V), which is directly related to its higher kinetic limitation (Figs. 2c and S4) due to low ionic conductivity of the EC/F-EMC electrolyte (Fig 1a). Both the faster evolution of the ASI (Fig. 4c) and the continuous growth of oxidation peaks at high voltages (Fig. 3c) originate mainly from severe electrolyte decomposition and the formation of unstable EEI layers during charging because of

Pursuant to the DOE Public Access Plan, this document represents the authors' peer-reviewed, accepted manuscript.
The published version of the article is available from the relevant publisher.

the relatively worse electrochemical stability (Fig. 1b). It is noteworthy that the percentage ratios of the first 1C-rate (fast rate) cycle capacity to the first C/10-rate (slow rate) cycle capacity (FC/SC ratio), for every 50 aging cycle term, indicates the degree of kinetic limitation in the cells (Fig. S4). The lower and gradually decreasing FC/SC ratio for the 1^{st} – 3^{rd} 50 aging cycle terms (up to 150 aging cycles) is related to its relatively high kinetic limitations in the EC/F-EMC cells (Fig. S4). During subsequent cycles, the FC/SC ratio sharply increases, which may be related to poor electrochemical stability of the EC/F-EMC electrolyte (Fig. 1c) and more lithium consumption and inventory loss by continuous electrolyte decomposition and unstable EEI formation during cycling at C/10, which has a longer charge/discharge time than the 1C, leading to a lower capacity during cycling at 1C.

In contrast, the relatively lower initial ASIs (Fig. S3) of the Gen2 electrolyte cell, especially at low voltages (< 2.1 V), compared with those of the EC/F-EMC electrolyte cell, may allow it to obtain additional capacity at low voltages (Fig. S5 and Table S1). The faster growth in impedance after 454 cycles (Fig. 4a) agrees well with the faster growth in polarization in the dQ/dV curves (Fig. 3a) after 400 cycles. The FC/SC ratio of the Gen2 electrolyte cell peaks in the 150^{th} cycle (0.95), and gradually decreases to 0.77 at the 955^{th} cycle. Both the increase in capacity differences of C/10 *vs*. 1C (Fig. 2C) and the decrease in the FC/SC ratio of every 50 aging cycle term suggest that the kinetic limitation is a detrimental factor resulting in gradual capacity fading.

On the other hand, for the FEC/EMC electrolyte cell, the relatively low impedance with slow growth rate (Fig. 4b) and the relatively high and stable CE (about 99.95% as shown in Fig. 2c) during cycling demonstrate that the cell has a relatively less significant kinetic limitation. In addition, a relatively small polarization is observed in the dQ/dV curves (Fig. 3b), which is consistent with the low impedance. The FC/SC ratio of the FEC/EMC electrolyte cell also keeps at a stable level (greater than 0.95) during the whole 1,000 cycles with an initial minor increase, which indicates much less kinetic limitations resulting in the best cyclability among the cells.

Pursuant to the DOE Public Access Plan, this document represents the authors' peer-reviewed, accepted manuscript. The published version of the article is available from the relevant publisher.

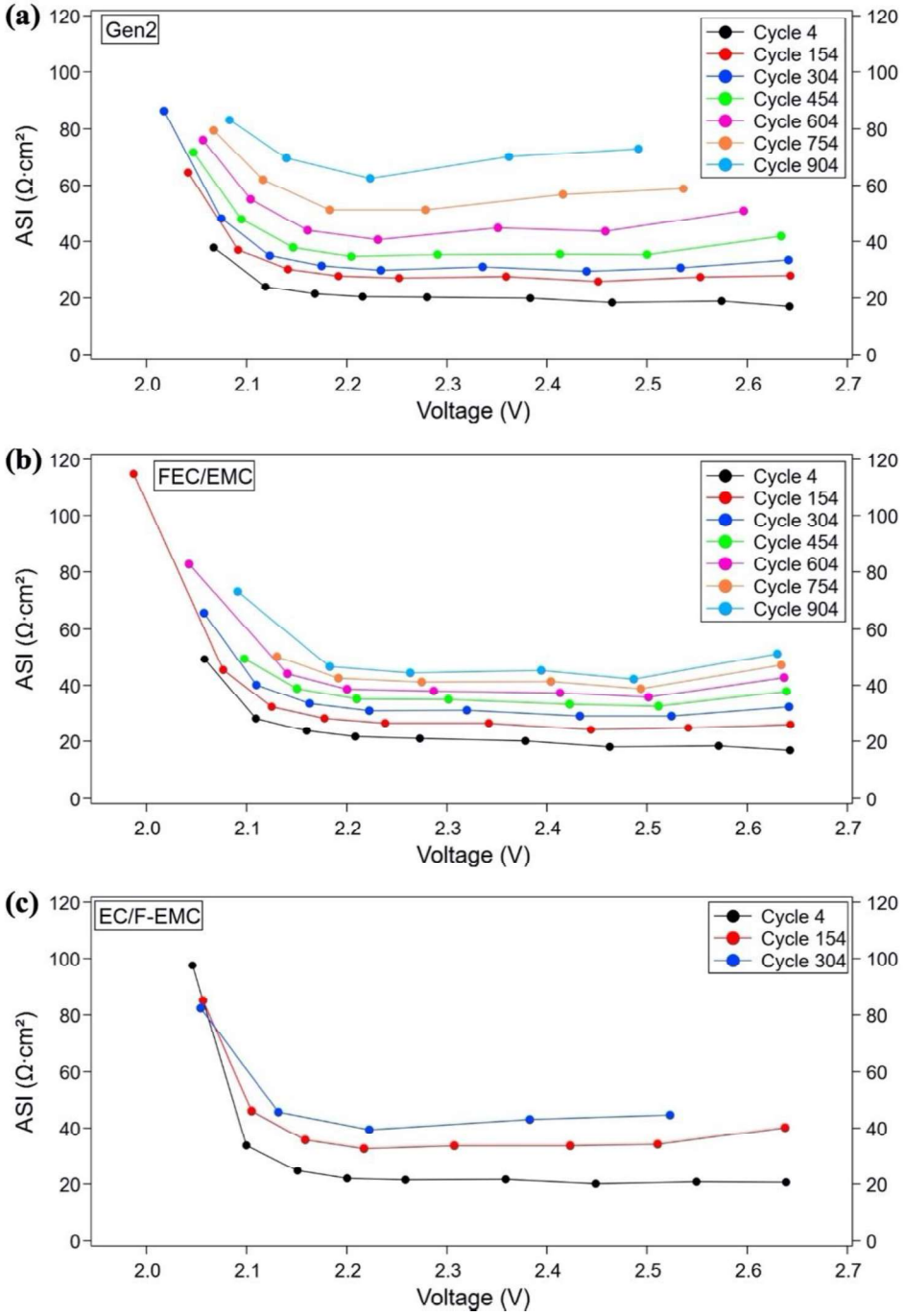

Figure 4. Evolution of areal specific impedance (ASI) plotted against the cell potentials upon cycling: (a) Gen2, (b) FEC/EMC and (c) EC/F-EMC electrolyte cells.

Cell failure mechanisms. Gradual capacity fading (Fig. 2c) with increasing ASI (Fig. 4) originates from either one or a combination of factors including continuous decomposition of an electrolyte, lithium inventory and/or active material loss, structural changes and/or mechanical failure of an electrode, loss of electronic contact of active materials and formation

Pursuant to the DOE Public Access Plan, this document represents the authors' peer-reviewed, accepted manuscript.
The published version of the article is available from the relevant publisher.

of a Li^+ ion-impermeable passivation layer on the electrodes. To verify which factors could be leading to the impedance growth and capacity fading in the cell upon cycling, additional half-cell cycling tests were performed using the electrodes retrieved from long-term cycled full cells with 3 different electrolytes (i.e., 1002 cycles for Gen2 electrolyte, 1002 cycles for FEC/EMC electrolyte and 206 cycles for EC/F-EMC electrolyte) and Li metal as a counter and reference electrode and compared to pristine half cells assembled with fresh working electrodes. The cycled LNMO//Li half cells were cycled in the voltage range of 3.0 – 4.25 V at C/10 (1C = 231 mAg^{-1}) with a voltage hold at 4.25 V at the end of charging (until the current drops below C/30). On the other hand, the cycled LTO//Li half cells were cycled in the voltage range of 1.0 – 2.5 V at C/10 (1C = 231 mAg^{-1}) with voltage holds at the ends of both charging and discharging (until the current drops below C/30).

In Fig. 5, the Gen2 and FEC/EMC half cells with cycled LNMO cathodes show 1st charge capacities of 129.9 and 116.4 $mAhg^{-1}$, respectively. For 1st discharge, however, the Gen2 half cell shows 136.4 $mAhg^{-1}$, which is only 6.5 $mAhg^{-1}$ higher than its 1st charge capacity, but 67.6 $mAhg^{-1}$ lower than the 1st discharge capacity of a pristine half cell with a new LNMO cathode. This indicates that loss of active materials is a dominant factor leading to capacity fade in the Gen2 full cells. In addition, the areas under the 3rd charge and discharge dQ/dV curves of the cell with the cycled cathode are much smaller than those of the cell with a pristine cathode, further demonstrating the apparent loss of active material in the cycled LNMO cathode with Gen2 electrolyte (Fig. S6a). In the case of the FEC/EMC half cell, during the 1st discharge, 174.6 $mAhg^{-1}$ of capacity is achieved, which is 58.2 $mAhg^{-1}$ higher than its 1st charge capacity and 24.7 $mAhg^{-1}$ lower than the 1st discharge capacity of the pristine half cell. Thus, compared to the electrochemical behaviors of the Gen2 full cells, active material loss may not be the main cause of capacity fade in FEC/EMC full cells. Instead, decrease of the H1 → M phase transition peaks (below 3.85 V) in the 1st charge and restoration of the oxidation peaks in later cycles of the dQ/dV curves (Fig. S6b) point to a large amount of lithium inventory loss in the FEC/EMC

Pursuant to the DOE Public Access Plan, this document represents the authors' peer-reviewed, accepted manuscript.
The published version of the article is available from the relevant publisher.

full cells. Finally, both pristine and cycled LNMO//Li half cells with EC/F-EMC electrolyte show much higher 1st charge capacities than cells with the other two electrolytes (Fig. 5c).

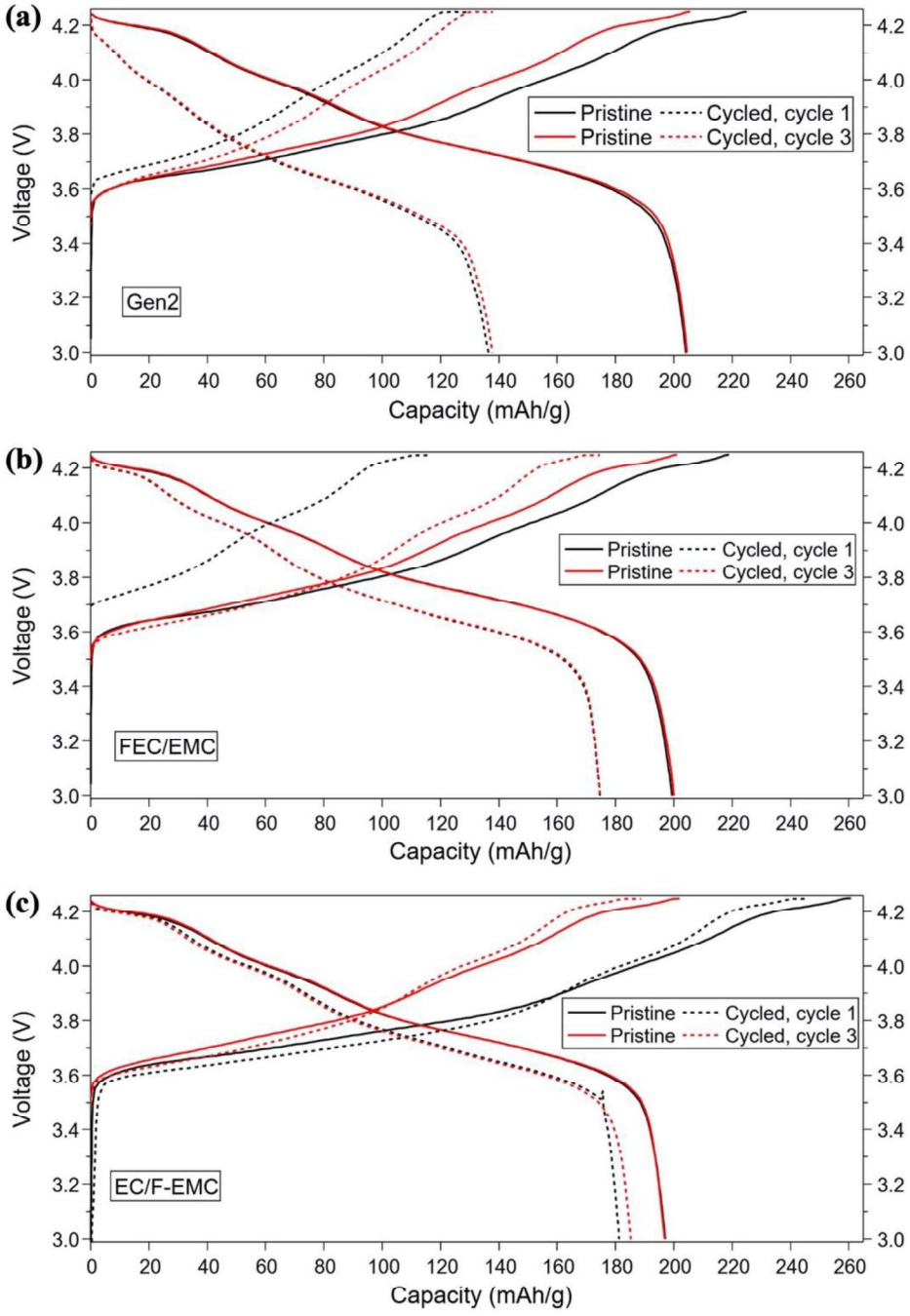

Figure 5. Specific capacity *vs*. voltage profiles of the pristine and cycled LNMO//Li half cells cycled in the voltage range of 3.0 – 4.25 V at C/10 (1C = 231 mAg^{-1}) with a voltage hold at the end of charging until the applied current ≤ C/30. The electrodes were retrieved from long-term cycled full cells with (a) Gen2, (b) FEC/EMC and (c) EC/F-EMC electrolytes.

Pursuant to the DOE Public Access Plan, this document represents the authors' peer-reviewed, accepted manuscript. The published version of the article is available from the relevant publisher.

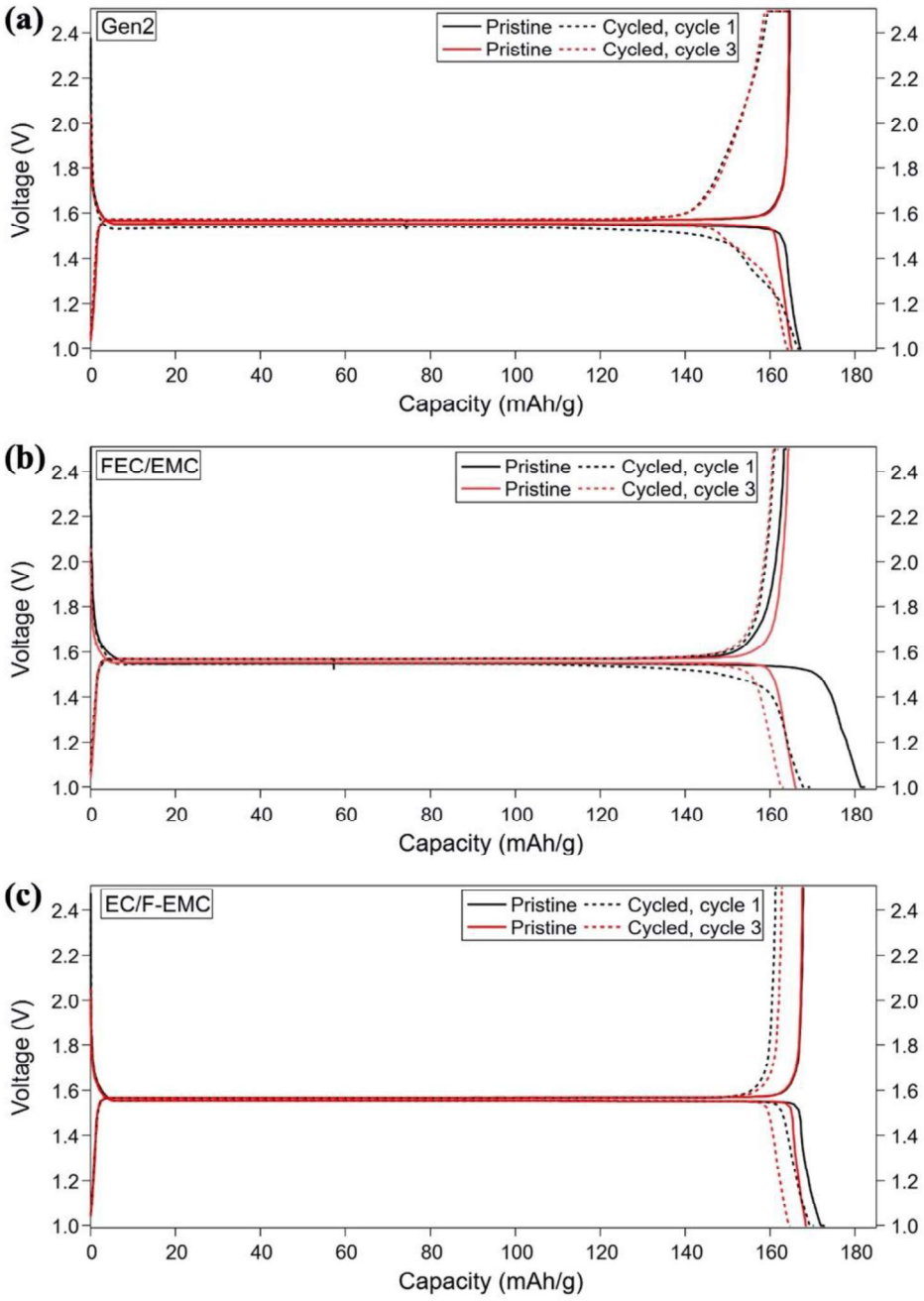

Figure 6. Specific capacity *vs*. voltage profiles of the pristine and cycled LTO//Li half cells cycled in the voltage range of 1.0 – 2.5 V at C/10 (1C = 231 mAg^{-1}) with voltage holds at the end of discharging and charging until the applied current ≤ C/30. The cycled electrodes were retrieved from long-term cycled full cells with (a) Gen2, (b) FEC/EMC and (c) EC/F-EMC electrolytes.

Specifically, both cells display relatively higher peak intensities in the voltage range of 3.55 – 3.9 V during 1st charge, compared to the Gen2 and FEC/EMC electrolyte half cells (Fig. S6c), indicating severe electrolyte decomposition due to low electrolyte stability (Fig. 1b) and unstable EEI formation. Similar reduction peak intensities in the EC/F-EMC half cells,

Pursuant to the DOE Public Access Plan, this document represents the authors' peer-reviewed, accepted manuscript.
The published version of the article is available from the relevant publisher.

compared with other two electrolyte cells, also support this conclusion. It is interesting there is less lithium inventory loss in the EC/F-EMC full cells, based on the similar 1st charge capacities of EC/F-EMC cells with cycled and pristine LNMO cathodes. Note that the cycled LNMO cathode was collected from the EC/F-EMC full cell after only 206 cycles due to its poor cycling performance (Fig. 2c). Considering the 3rd discharge capacity difference (~12 $mAhg^{-1}$) of the half cells with pristine (196.8 $mAhg^{-1}$) *vs*. cycled (185.2 $mAhg^{-1}$) LNMO cathodes, active material loss may not be the main cause of capacity fading with a drastic CE drop.

The specific capacity *vs*. voltage profiles of the LTO//Li half cells with cycled LTO anodes collected from full cells with Gen2 (1002 cycles), FEC/EMC (1002 cycles) and EC/F-EMC (206 cycles) electrolytes are shown in Fig. 6. Both the Gen2 and FEC/EMC electrolyte half cells with LTO anodes retrieved after 1002 cycles show similar specific capacities compared to those of the half cells with pristine LTO anodes, except the 1st discharge capacity of the pristine LTO//Li half cell with FEC/EMC electrolyte, which suggests limited active material loss for LTO anodes in both cells (Figs. 6a and 6b). Extra capacity during the 1st discharge of the FEC/EMC half cell with the pristine LTO anode is possibly due to electrolyte decomposition and SEI formation on the LTO surface, and increase of CE upon cycles (89.86% for the 1st cycle → 98.31% for the 3rd cycle) indicates formation of a stable SEI layer. It is noteworthy that the Gen2 electrolyte half cell with the cycled LTO anode shows relatively less steep curves at both ends of charge and discharge and additional capacities from the CV steps after the 1st and 3rd charges (Fig. 6a). The FEC/EMC electrolyte half cell with the cycled LTO anode, however, displays minor differences in end-of-curve steepness and CV hold capacities compared to those of the pristine cell (Fig. 6b). One possible explanation for the observation is that the LTO electrode in Gen2 electrolyte full cells may form a more resistive SEI layer that may cause impedance growth during long-term cycling. For the EC/F-EMC electrolyte half cells, less than 5 $mAhg^{-1}$ of active material may be lost from the LTO anode during 206 cycles, based on capacity differences between the LTO half cells with pristine and cycled electrodes

Pursuant to the DOE Public Access Plan, this document represents the authors' peer-reviewed, accepted manuscript.
The published version of the article is available from the relevant publisher.

(Fig. 6c). In addition, a negligible difference in end-of-curve steepness of pristine and cycled LTO half cells suggests a less resistive SEI layer is formed on the LTO anode after 206 cycles in the EC/F-EMC electrolyte. Despite the moderate degradation of the cycled LTO electrode with EC/F-EMC, however, the severe electrolyte decomposition and unstable EEI formation during charging (Fig. 5c) still causes faster capacity fading of the cell.

2.3. Post-mortem Analysis

Utilizing electron- and X-ray-based characterization techniques, such as scanning electron microscopy (SEM) with energy dispersive X-ray spectroscopy (EDS), cryogenic transmission electron microscopy (cryo-TEM) and X-ray photoemission spectroscopy (XPS), the surface morphology, elemental distribution and surface chemistry of pristine and cycled electrodes were characterized to better understand the electrochemical analysis and diagnostics.

Surface morphology and elemental distribution. Figs S7 and S8 show SEM images (15 μm and 1 μm scales, respectively) of cycled LTO electrodes after formation and long-term cycling in the three different electrolytes. After two formation cycles in Gen2 and FEC/EMC electrolytes, no significant change is observed on the LTO surface (Figs. S7a and S7b) compared to the pristine anode (Fig. S9a) at a large scale (15 μm). In addition, sharp surfaces are visible at a smaller scale (1 μm) in Figs. S8a and S8b suggesting no significant SEI layer is produced after formation cycles. After 1002 cycles, however, island-like dots—possibly separated SEI layers—are observed on the LTO surface cycled in both Gen2 and FEC/EMC electrolytes (Figs. S8d and S8e), while there are negligible changes to the anodes at a large scale (Figs. S7d and S7e). Specifically, the LTO anode after 1002 cycles in the FEC/EMC electrolyte shows fewer dot-like features than that cycled in the Gen2 electrolyte, suggesting less (or possibly thinner) SEI layers formed after long-term cycling. This may explain better the kinetics, lower impedance and less polarization of the FEC/EMC electrolyte cells compared to the Gen2 electrolyte cells observed in electrochemical tests (Figs. 2-4 and 6). In the case of the EC/F-

Pursuant to the DOE Public Access Plan, this document represents the authors' peer-reviewed, accepted manuscript.
The published version of the article is available from the relevant publisher.

EMC electrolyte, many more regions of the porous structure of the LTO electrode are clogged in the long-term cycled LTO (Fig. S7f), compared to the LTO after formation (Fig. S7c), at a large scale, indicating thick SEI layers. Note that the island-like dots are observed only after formation cycles (Fig. S8c), whereas those features disappear in long-term cycled anode (Fig. S8f), possibly due to formation of thicker SEI layers that may cause the poorer kinetics and higher impedance of the cells (Figs. 2-4 and 6).

SEM images of the LNMO electrodes after formation and long-term cycling in the three different electrolytes are shown in Figs. S10 and S11. With the Gen2 and FEC/EMC electrolytes, there is a negligible change in structure after formation cycling (Figs. S11a and S11b) compared to the pristine LNMO electrode (Fig. S9d). After long-term cycling (Figs. S11d and S11e), however, the LNMO particles are apparently covered with CEI layers. For the EC/F-EMC electrolyte cell, the LNMO particles are covered with CEI layers even after formation cycling (Fig. S11c) and similar morphologies are observed after long-term cycling (Fig. S11f).

EDS spectra of the LTO and LNMO electrodes before cycling and after formation or long-term cycling are shown in Figs S12 and S13, respectively. Compared to the pristine LTO anode, formation cycled LTO electrodes in the three electrolytes show little increase in the intensities of phosphorus (P) peaks (Figs. S12b, S12d and S12f) suggesting that a limited amount of P-containing SEI components was formed. After long-term cycling, the intensities of P peaks grow to similar extends in all electrolytes (Figs. S12c, S12e and S12g), indicating a more P-rich SEI is formed after long-term cycling. It is noteworthy that the SEI growth rate in EC/F-EMC electrolyte is faster than in other electrolytes given that the cycled LTO anode from the EC/F-EMC cell has been collected much earlier (347 cycles) than others (1002 cycles). Negligible Ni signals for all long-term cycled LTO anodes indicate a limited amount of Ni is dissolved, cross-talked and deposited on the LTO anodes, possibly due to stable CEI layers formed on LNMO cathodes.

Pursuant to the DOE Public Access Plan, this document represents the authors' peer-reviewed, accepted manuscript.
The published version of the article is available from the relevant publisher.

After formation cycles, all LNMO cathodes show even lower P intensities, compared with formation cycled LTO anodes, indicating formation of less P-rich CEI layers (Figs. S13b, S13d and S13f). Similar to the long-term cycled LTO anodes, an increase of P peak intensities in long-term cycled LNMO cathodes may suggest formation of a P-rich CEI upon cycling with a relatively faster CEI growth rate in the EC/F-EMC electrolyte (Figs. S13c, S13e and S13g).

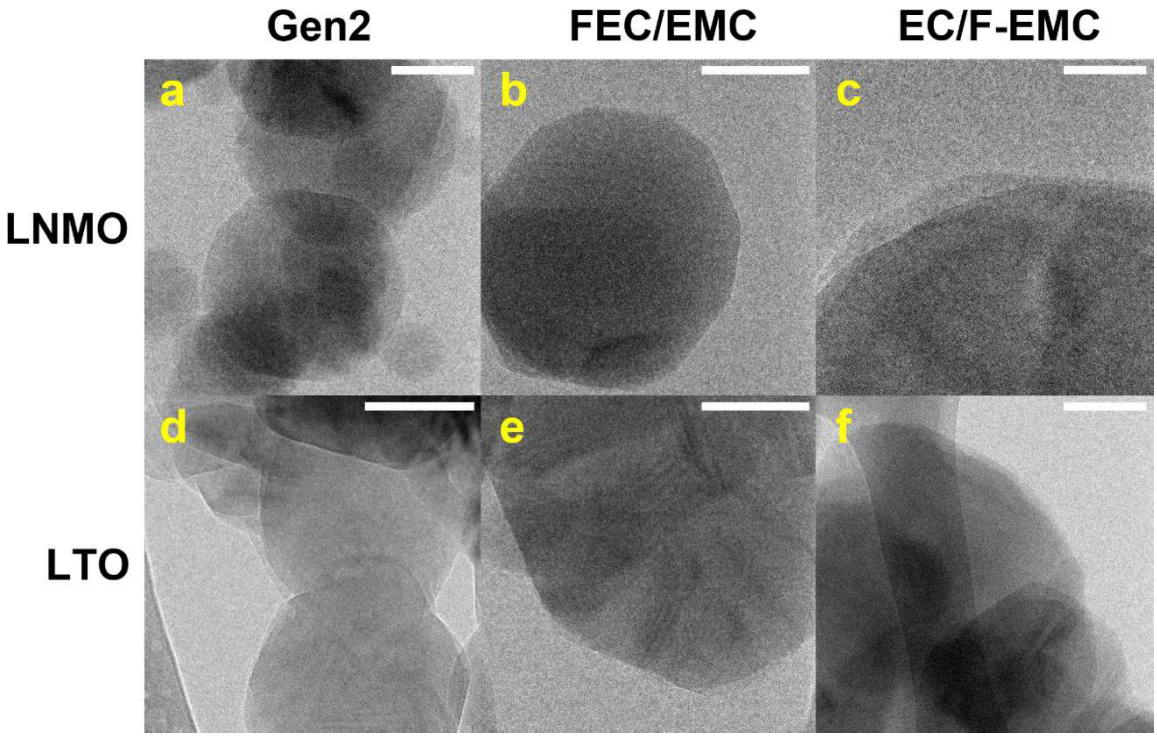

Figure 7. Cryo-TEM images of (a-c) LNMO cathodes and (d-f) LTO anodes from long-term cycled full cells with the Gen2 (1002 cycles, a & d), FEC/EMC (1002 cycles, b & e), and EC/F-EMC (347 cycles, c & f) electrolytes. Scale bars are 100 nm.

Fig. 7 shows cryo-TEM images of long-term cycled LNMO and LTO electrodes with the three electrolytes. For the LTO anode after 1002 cycles in the Gen2 electrolyte, some particles within the LTO anode were covered with a thin SEI layer (Fig. 7d) compared to those in the pristine anode (Fig. S14b). Not all particles showed this layer, however, and negligible (or very thin) CEI layers were observed on the surface of the LNMO particles cycled in Gen2 (Fig. 7a). The situation was similar with FEC/EMC electrolyte after 1002 cycles, where heterogeneously formed thin SEI layers were observed on some LTO particles (Fig. 7e), whereas many LNMO

Pursuant to the DOE Public Access Plan, this document represents the authors' peer-reviewed, accepted manuscript.
The published version of the article is available from the relevant publisher.

particles retained a smooth, featureless surface (Fig. 7b). In some cases, these SEI layers on some LTO particles were already observed after formation cycles (Figs. S15d and S15e). The heterogeneity of these layers may represent a closer view of the island dot-like features observed in SEM images (Fig. S8b).

With EC/F-EMC electrolyte, the surface morphology was more distinct. A thin CEI layer was observed uniformly coating LNMO particles after formation (Fig. S15c), with relatively thicker and less uniform layers observed after 347 cycles (Fig. 7c). The LTO particle surfaces were less consistently altered by cycling but still showed thin, non-uniform SEI layers after 347 cycles (Fig. 7f). This mirrored the SEM data, where the LNMO cathode already showed CEI layers after formation cycles (Fig. S11c) with similar morphologies after long-term cycles (Fig. S11f).

Surface chemistry. High-resolution core-level XPS analysis was conducted to investigate the surface chemistry of pristine and cycled LTO and LNMO electrodes collected from full cells with three different electrolytes as shown in Figs. 8, 9, S16 and S17. Two distinct peaks at around 459.5 eV and 465.2 eV in the Ti 2p spectra were assigned to Ti^{4+} $2p_{1/2}$ and $2p_{3/2}$ states from LTO (Fig. 8a).[52] After formation cycles, intensities of the Ti peaks for all cycled LTO anodes from the three different electrolyte cells were decreased to similar levels due to SEI formation. After long-term cycling, it was apparent that both Ti peaks for the LTO anode cycled in EC/F-EMC electrolyte almost diminished, indicating a relatively thick SEI layer was formed due to continuous electrolyte decomposition. Considering the limited surface analysis depth (5-10 nm) of XPS ($h\upsilon$ = 1.487 keV)[10,53] and the cryo-TEM results (Fig. 7f), however, the coated SEI layers on the LTO surface may be non-uniform. On the other hand, minor changes in Ti peak intensities were observed for LTO anodes cycled in Gen2 or FEC/EMC electrolyte, suggesting relatively thin SEI layers were formed.

Pursuant to the DOE Public Access Plan, this document represents the authors' peer-reviewed, accepted manuscript.
The published version of the article is available from the relevant publisher.

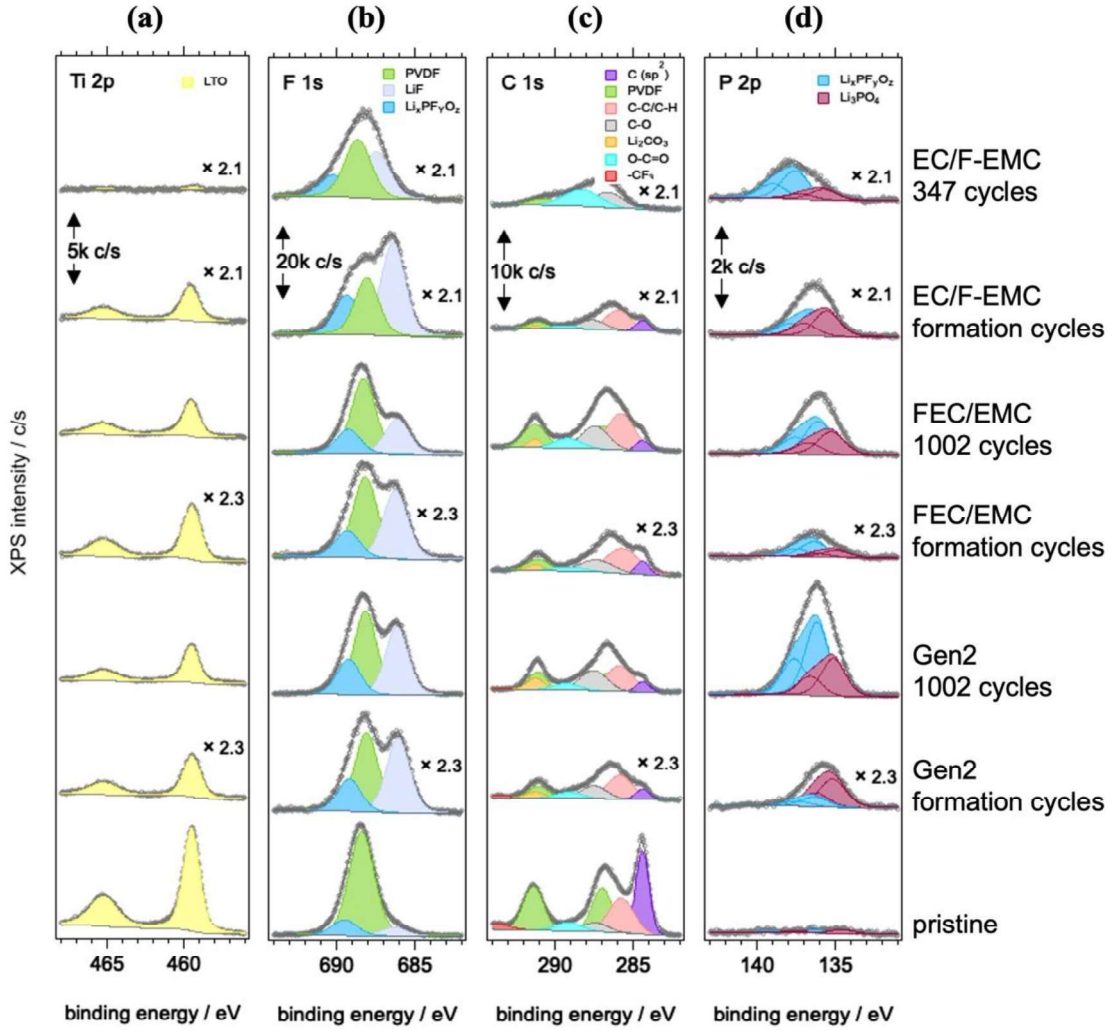

Figure 8. High-resolution (a) Ti 2p, (b) F 1s, (c) C 1s, and (d) P 2p core-level XPS spectra of pristine and cycled LTO anodes collected from formation and long-term cycled full cells in Gen2, FEC/EMC, and EC/F-EMC electrolytes.

For the F 1s core-level XPS spectra (Fig. 8b) the intensity of LiF peak at around 686.3 eV for the LTO anode after long-term cycling in FEC/EMC electrolyte decreased compared to the anode after formation cycles,[10] while there was no significant change in LiF peak intensity for formation cycled *vs*. long-term cycled LTO anodes from the Gen2 cell. This could be due to dense, LiF-rich SEI inner layers forming during formation cycles in the fluorinated solvent-based electrolyte that may effectively prevent further electrolyte decomposition.[54] LiF species could be dissolved and/or detached from the electrode surface during subsequent cycles, but the former explanation is preferred considering its low solubility[55,56] and good stability[56-58].

Pursuant to the DOE Public Access Plan, this document represents the authors' peer-reviewed, accepted manuscript.
The published version of the article is available from the relevant publisher.

In the case of Gen2 electrolyte, a relatively less dense SEI inner layer may be formed during formation cycles that may not effectively protect the LTO electrode. Additional electrolyte decomposition may occur, leading to the formation of a less dense, P-rich outer SEI layer upon subsequent cycles (Fig. 8d). Increases in $Li_xPF_yO_z$ and Li_3PO_4 peak intensities at around 136 and 135 eV in P 2p spectra of the long-term cycled LTO anodes from Gen2 cell, compared to formation cycled ones, suggest additional $LiPF_6$ salt decomposition may occur and less dense, P-rich outer SEI layers were formed upon cycling (Fig. 8d).[59-61] In the case of LTO anode after long-term cycling in the EC/F-EMC electrolyte, the $Li_xPF_yO_z$ peak was shifted to higher binding energy, suggesting that the lithium fluorophosphate species became more F-rich, possibly due to further salt decomposition.[59] It is noteworthy that the LTO anode after long-term cycling in the EC/F-EMC electrolyte shows a relatively higher intensity of the O-C=O peak at around 289 eV in the C 1s spectra, corresponding to carboxylate species originating from electrolyte solvent decomposition (Fig. 8c).[62,63]

Interestingly, the cycled LNMO electrodes from FEC/EMC and Gen2 cells show similar XPS spectra in terms of peak position (specific CEI component), peak intensity ratios (specific CEI composition) and peaks growth trends (CEI evolution) upon cycling (Fig. 9). Such similarities indicate that FEC may have a limited influence on CEI formation and evolution of layered oxide cathodes in a moderate voltage window.[34] On the other hand, the formation and long-term cycled LNMO electrodes from the EC/F-EMC cell show negligible changes in XPS spectra. Specifically, a limited amount of lithium phosphate and fluorophosphate species were formed after limited long-term cycling (347 cycles) as shown in the P 2p spectra (Fig. 9c). In addition, other CEI species, such as carboxylate (O-C=O), alkoxide (C-O)[62] and lithium carbonate (Li_2CO_3) in the C 1s spectra (Fig. 9b) and LiF in the F 1s spectra (Fig. 9a), are at low levels compared to the cycled electrodes from Gen2 and FEC/EMC cells. The stable and limited amount of CEI species in the EC/F-EMC cell suggest a relatively stable and dense CEI layer may be formed. The relatively low intensities of LiF peaks in the F 1s spectra of cycled LNMO

Pursuant to the DOE Public Access Plan, this document represents the authors' peer-reviewed, accepted manuscript.
The published version of the article is available from the relevant publisher.

electrodes from EC/F-EMC cells suggest the formation of a stable and dense CEI layers is probably more related to EC rather than F-EMC. The high content of EC (70%) in the EC/F-EMC electrolytes may be responsible for the formation of stable and dense CEI layer, as EC is known to form poly (ethylene carbonate) films on the cathode surface at high voltages.[64] The stable and dense CEI layer could explain the relatively less active material loss in the cycled LNMO cathode and negligible Ni signal on the cycled LTO anode from EC/F-EMC cell (Figs. 5c and S12).

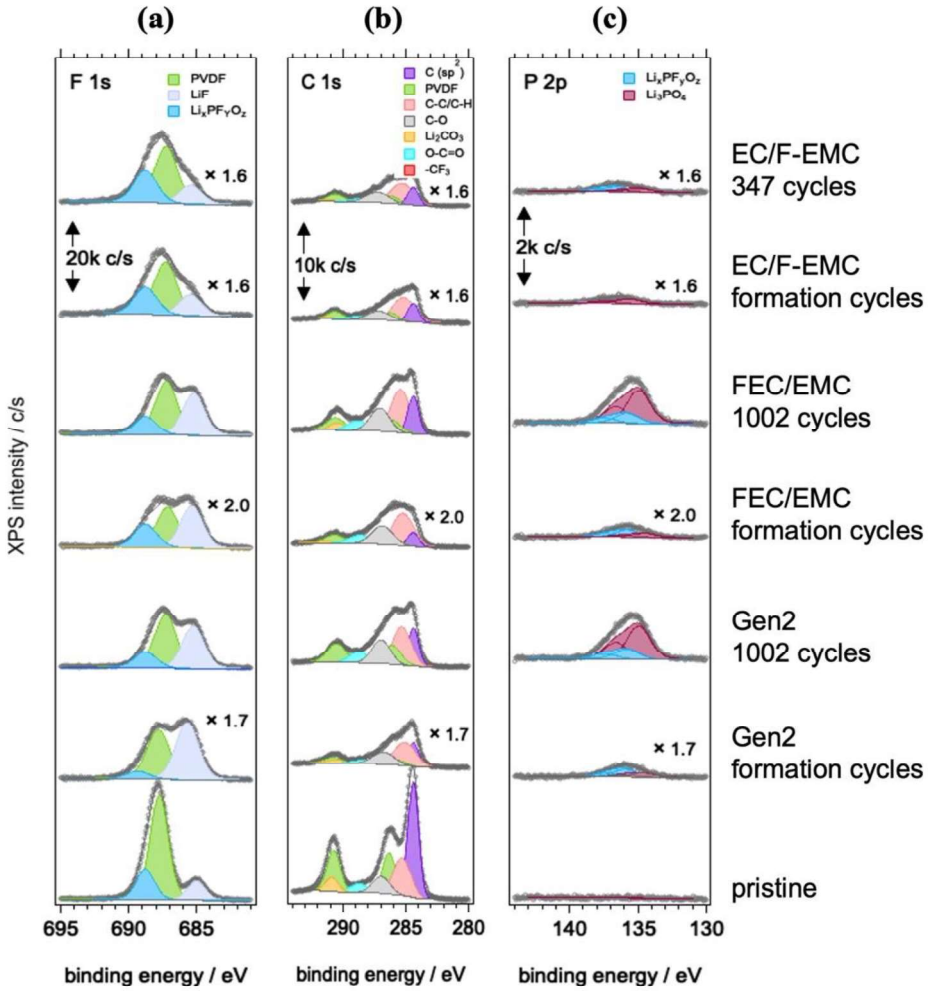

Figure 9. High-resolution (a) F 1s, (b) C 1s, and (c) P 2p core-level XPS spectra of pristine and cycled LNMO cathodes collected from formation and long-term cycled full cells in Gen2, FEC/EMC, and EC/F-EMC electrolytes.

Pursuant to the DOE Public Access Plan, this document represents the authors' peer-reviewed, accepted manuscript. The published version of the article is available from the relevant publisher.

3. Conclusion

In this study, we evaluated and analyzed electrochemical performance and behaviors of two different fluorinated solvent-based electrolytes—1.0 M $LiPF_6$ in FEC:EMC (3:7 wt.%) (FEC/EMC) and 1.0 M $LiPF_6$ in EC:F-EMC (7:3 wt.%) (EC/F-EMC) compared with the Gen2 electrolyte—in a $Li_4Ti_5O_{12}$ (LTO)//$LiNi_{0.9}Mn_{0.1}O_2$ (LNMO) full cell chemistry at 45°C for BTMS applications. We found that the FEC/EMC electrolyte cell outperformed the Gen2 electrolyte cell over 1000 long-term cycles (at 1C in the voltage range of 1.4 – 2.7 V) with 57.9% capacity retention and 99.96% CE compared to 46.8% capacity retention and 99.92% CE in the Gen2 electrolyte cell. The failure mechanisms and aging behaviors of the cells with the three different electrolytes were systematically studied utilizing a combination of electrochemical testing and diagnostics (e.g., dQ/dV, ASI, CV hold and rate capability) and post-mortem characterization (e.g., SEM, cryo-TEM and XPS). Capacity fading in the Gen2 electrolyte cell was found to originate from a continuous increase in cell impedance due to resistive SEI layers formed on the LTO anode. Furthermore, the high cell impedance resulted in low CE, high overpotential, Li trapping in the anode and cathode active material loss. Cells with the EC/F-EMC electrolyte showed the fastest capacity fade with low reversible capacity and CE because of severe and continuous electrolyte decomposition due to the lowest electrochemical stability of EC/F-EMC electrolyte at 45°C and unstable SEI layer formed. On the other hand, the FEC/EMC electrolyte cell exhibited a stable, high CE (>99.95%) and low cell impedance with a slow growth rate, mainly due to a dense, stable and less resistive LiF-rich SEI layer formed on LTO during formation cycles that mitigated further electrolyte decomposition upon aging cycles. We believe the knowledge obtained from these fundamental and mechanistic studies will allow for rational design of new electrode chemistries and electrolyte formulations for the development of BTMS rechargeable batteries with enhanced safety, longer lifespan and higher energy density at 45°C.

Pursuant to the DOE Public Access Plan, this document represents the authors' peer-reviewed, accepted manuscript.
The published version of the article is available from the relevant publisher.

4. Experimental Section

Electrolyte Preparation and Properties Analysis. The reference Gen2 electrolyte—1.2 M lithium hexafluorophosphate ($LiPF_6$) in ethylene carbonate (EC):ethyl methyl carbonate (EMC) (3:7 wt.%)—was purchased from Tomiyama Pure Chemical Industries. Other two different electrolytes, 1.0 M $LiPF_6$ (>99.99%, Sigma Aldrich) in fluoroethylene carbonate (FEC, Tomiyama):EMC (Tomiyama) (3:7 wt.%) (FEC/EMC) and 1.0 M $LiPF_6$ in EC (Gotion):methyl (2,2,2-trifluoroethyl) carbonate (F-EMC, >99.5%, Argonne's Materials Engineering Research Facility) (7:3 wt.%) (EC/F-EMC) were prepared in an Ar-filled glove box (VAC) in which the water and oxygen content was kept at less than 0.2 and 0.5 ppm, respectively.

Water contents of the electrolytes were measured using a Karl Fischer titrators (ETTLER TOLEDO C20S) located inside a glove box, and the values of all electrolytes were less than 10 ppm. Ionic conductivity of the electrolytes was measured using an AMEL digital conductivity meter (MOD 2131). The conductivity values were recorded from 25°C (room temperature, RT) to 55°C with the step of 10°C. Linear sweep voltammetry measurements were conducted with a three-electrode cell inside the glovebox using a BioLogic potentiostat at RT and 45°C. Lithium wires (Sigma Aldrich, ≥ 98%, 3.2 mm in diameter) polished with a sandpaper were used as the reference and counter electrodes and a platinum disk (CH Instruments, 2.0 mm in diameter) was used as the working electrode.

Electrodes and Cell Fabrication. Both $LiNi_{0.9}Mn_{0.1}O_2$ (LNMO) and $Li_4Ti_5O_{12}$ (LTO) electrodes were provided by Cell Analysis, Modeling and Prototyping (CAMP) Facility at Argonne National Laboratory. The NM90-10 electrode containing 90 wt.% active material, 5 wt.% carbon black (Timcal C45) and 5 wt.% polyvinylidene fluoride binder (PVDF, Solvay 5130) was coated on an Al foil (20 μm) with the loading of 9.63 mg cm^{-2}. The LTO electrode containing 87 wt.% LTO (Samsung Fine Chemicals Company), 5 wt.% carbon black (Timcal

Pursuant to the DOE Public Access Plan, this document represents the authors' peer-reviewed, accepted manuscript.
The published version of the article is available from the relevant publisher.

C45) and 8 wt% PVDF (Kureha 9300) was coated on an Al foil (20 μm) with the loading of 14.1 mg cm^{-2}.

CR2032 coin-type cells were assembled in the Ar-filled glove box. Cathodes (14 mm diameter), anodes (15 mm diameter), separators (Celgard 2325, 19 mm diameter) and 50 μL electrolyte were used to assemble the cells. Instead of Celgard 2325, Dreamwever Gold separator was used for the EC/F-EMC electrolyte since the electrolyte does not wet on Celgard 2325. For precise electrode alignment in a full cell, the electrodes were welded to the stainless-steel spacers before cell assembly. The N/P ratio of the full cell with those electrodes was 1.07. A polished and punched Li metal foil (99.9%, 0.75 mm thick, Alfa Aesar) was used as an anode in a half cell.

Electrochemical Cell Tests. All cells were tested in the MACCOR MTC-020 temperature chamber (at 45 °C) connected to a MACCOR Series 4000 Automated Test System. The cells were rested at OCV for 12 hours before tests for enough wetting of the electrodes. A combined galvanostatic cycling and area-specific impedance (ASI) measurement protocol was employed to check the impedance changes upon cycling. Initial two formation cycles were performed at C/10 (1C = 231 mA g^{-1}) in the voltage range of 1.4 – 3.0 V with a constant voltage (CV) at the end of constant current (CC) charge step (until the current dropped below C/30). After formation cycles, the cells were cycled at 1C in the voltage range of 1.4 – 2.7 V with a constant voltage hold at the end of CC charge until the current was lower than C/20. ASI tests were performed afterwards based on a specific protocol: cells were first discharged at 1C until 1/10 of the 1C capacity (195 mAh g^{-1}). After a 1-hour rest, a 10-second 2C discharge pulse was applied to measure a voltage drop. Cells were rested for 40 seconds after the discharge pulse. A 10-second 1.5C recovery charge pulse was then applied to cells followed by a 40-second rest. The ASI protocol was then repeated for 10 times or until the voltage dropped below 0.9 V during the 10-second discharge pulse. Cells were then discharged to 1.4 V at 1C with a voltage hold until C/20 to complete the discharge process. The subsequent 48 aging cycles were

Pursuant to the DOE Public Access Plan, this document represents the authors' peer-reviewed, accepted manuscript.
The published version of the article is available from the relevant publisher.

performed after each ASI test. Specifically, in the 48th 1C aging cycle, a voltage hold at 1.4 V (until applied current ≤ C/20) was added at the end of discharging. A set of 50 cycles—one C/10 cycle, one ASI cycle and forty eight 1C cycles—was repeated 20 times. Electrochemical cycling tests were stopped either after 1000 aging cycles or when the CE was lower than 70%.

Post-Mortem Analyses and Data Processing. After electrochemical tests, cells were disassembled in the glove box to collect electrodes for post-mortem analyses including SEM, XPS and cryo-TEM. The retrieved electrodes were rinsed with 5 mL of dimethyl carbonate (DMC) for 2 min and vacuum dried in the antechamber of glovebox for 1 hour before characterizations. SEM images were obtained by a Hitachi S-4800 SEM operated at an acceleration voltage of 6 kV and a current of 5 μA. Samples for cryo-TEM were prepared in an argon-atmosphere glovebox by gently scraping the surface of the electrodes with a razor blade, then rubbing the surface with a copper TEM grid with a lacey carbon substrate to collect the loosened particles. Grids were sealed in an Eppendorf tube, removed from the glovebox, and plunged in liquid nitrogen (LN2). While submerged in LN2, the tube was broken to retrieve the sample without exposure to atmosphere as in reference 50.[65] Samples were transferred to the TEM (FEI Tecnai ST30) using a Gatan 626 cryo-transfer holder. Samples were imaged at 300kV, with the temperature stable below -170°C. XPS measurements were performed by a Physical Electronics 5600 X-ray photoelectron spectrometer with monochromatic Al Kα X-ray excitation ($h\nu$ = 1.487 keV). A custom program based on Igor Pro software previously described[66] was used for data processing and curve fitting.

Pursuant to the DOE Public Access Plan, this document represents the authors' peer-reviewed, accepted manuscript.
The published version of the article is available from the relevant publisher.

Declaration of Competing Interests

The authors declare that they have no known competing financial interests or personal relationships that could have appeared to influence the work reported in this paper.

Acknowledgements

This work was authored by the National Renewable Energy Laboratory, operated by Alliance for Sustainable Energy, LLC, for the U.S. Department of Energy (DOE) under Contract No. DE-AC36-08GO28308. Funding provided by the U.S. DOE's Vehicle Technologies Office (VTO) under the Behind-the-Meter Storage Consortium directed by Samuel Gillard and managed by Anthony Burrell. Support from the VTO, Hybrid Electric Systems Program, David Howell (Manager), Battery R&D, Peter Faguy (Technology Manager), at the U.S. DOE, Office of Energy Efficiency and Renewable Energy, is gratefully acknowledged. The electrodes used in this manuscript are from Argonne's Cell Analysis, Modeling and Prototyping (CAMP) Facility, which is fully supported by the DOE VTO. The views expressed in the article do not necessarily represent the views of the DOE or the U.S. Government. The U.S. Government retains and the publisher, by accepting the article for publication, acknowledges that the U.S. Government retains a nonexclusive, paid-up, irrevocable, worldwide license to publish or reproduce the published form of this work, or allow others to do so, for U.S. Government purposes.

Pursuant to the DOE Public Access Plan, this document represents the authors' peer-reviewed, accepted manuscript. The published version of the article is available from the relevant publisher.

References

[1] X. Shuai, R. Raufer, Behind-the-meter energy storage in China: Lessons from California's approach, WIREs Energy and Environment. 10 (2021) e394. https://doi.org/10.1002/wene.394.

[2] Y. Yang, E.G. Okonkwo, G. Huang, S. Xu, W. Sun, Y. He, On the sustainability of lithium ion battery industry – A review and perspective, Energy Storage Materials. 36 (2021) 186–212. https://doi.org/10.1016/j.ensm.2020.12.019.

[3] O. Schmidt, A. Hawkes, A. Gambhir, I. Staffell, The future cost of electrical energy storage based on experience rates, Nat Energy. 2 (2017) 1–8. https://doi.org/10.1038/nenergy.2017.110.

[4] A. Odukomaiya, A. Abu-Heiba, B. Bekker, The Value of Behind-The-Meter Energy Storage for Buildings: A Case Study on a University Building in South Africa, in: 2018 IEEE PES/IAS PowerAfrica, IEEE, Cape Town, 2018: pp. 640–645. https://doi.org/10.1109/PowerAfrica.2018.8521100.

[5] M. Li, J. Lu, Cobalt in lithium-ion batteries, Science. 367 (2020) 979–980. https://doi.org/10.1126/science.aba9168.

[6] J. Wang, P. Liu, J. Hicks-Garner, E. Sherman, S. Soukiazian, M. Verbrugge, H. Tataria, J. Musser, P. Finamore, Cycle-life model for graphite-$LiFePO_4$ cells, Journal of Power Sources. 196 (2011) 3942–3948. https://doi.org/10.1016/j.jpowsour.2010.11.134.

[7] K. Zaghib, M. Dontigny, A. Guerfi, P. Charest, I. Rodrigues, A. Mauger, C.M. Julien, Safe and fast-charging Li-ion battery with long shelf life for power applications, Journal of Power Sources. 196 (2011) 3949–3954. https://doi.org/10.1016/j.jpowsour.2010.11.093.

[8] W.-J. Zhang, Structure and performance of $LiFePO_4$ cathode materials: A review, Journal of Power Sources. 196 (2011) 2962–2970. https://doi.org/10.1016/j.jpowsour.2010.11.113.

[9] B. Zhao, R. Ran, M. Liu, Z. Shao, A comprehensive review of $Li_4Ti_5O_{12}$-based electrodes for lithium-ion batteries: The latest advancements and future perspectives, Materials Science and Engineering: R: Reports. 98 (2015) 1–71. https://doi.org/10.1016/j.mser.2015.10.001.

[10] Y. Ha, S.P. Harvey, G. Teeter, A.M. Colclasure, S.E. Trask, A.N. Jansen, A. Burrell, K. Park, Long-term cyclability of $Li_4Ti_5O_{12}/LiMn_2O_4$ cells using carbonate-based electrolytes for behind-the-meter storage applications, Energy Storage Materials. 38 (2021) 581–589. https://doi.org/10.1016/j.ensm.2021.03.036.

[11] T. Ohzuku, A. Ueda, N. Yamamoto, Zero- Strain Insertion Material of $Li[Li_{1/3}Ti_{5/3}]O_4$ for Rechargeable Lithium Cells, J. Electrochem. Soc. 142 (1995) 1431–1435. https://doi.org/10.1149/1.2048592.

[12] J. Guo, W. Zuo, Y. Cai, S. Chen, S. Zhang, J. Liu, A novel $Li_4Ti_5O_{12}$-based high-performance lithium-ion electrode at elevated temperature, J. Mater. Chem. A. 3 (2015) 4938–4944. https://doi.org/10.1039/C4TA05660D.

[13] G.-N. Zhu, H.-J. Liu, J.-H. Zhuang, C.-X. Wang, Y.-G. Wang, Y.-Y. Xia, Carbon-coated nano-sized $Li_4Ti_5O_{12}$ nanoporous micro-sphere as anode material for high-rate lithium-ion batteries, Energy & Environmental Science. 4 (2011) 4016–4022. https://doi.org/10.1039/C1EE01680F.

[14] Z. Yang, D. Choi, S. Kerisit, K.M. Rosso, D. Wang, J. Zhang, G. Graff, J. Liu, Nanostructures and lithium electrochemical reactivity of lithium titanites and titanium oxides: A review, Journal of Power Sources. 192 (2009) 588–598. https://doi.org/10.1016/j.jpowsour.2009.02.038.

[15] E. Rossen, C.D.W. Jones, J.R. Dahn, Structure and electrochemistry of $Li_xMn_yNi_{1-y}O_2$, Solid State Ionics. 57 (1992) 311–318. https://doi.org/10.1016/0167-2738(92)90164-K.

[16] Y. Makimura, T. Ohzuku, Lithium insertion material of $LiNi_{1/2}Mn_{1/2}O_2$ for advanced lithium-ion batteries, Journal of Power Sources. 119–121 (2003) 156–160. https://doi.org/10.1016/S0378-7753(03)00170-8.

Pursuant to the DOE Public Access Plan, this document represents the authors' peer-reviewed, accepted manuscript. The published version of the article is available from the relevant publisher.

[17] S. Gopukumar, K.Y. Chung, K.B. Kim, Novel synthesis of layered $LiNi_{1/2}Mn_{1/2}O_2$ as cathode material for lithium rechargeable cells, Electrochimica Acta. 49 (2004) 803–810. https://doi.org/10.1016/j.electacta.2003.09.034.
[18] J. Bréger, Y.S. Meng, Y. Hinuma, S. Kumar, K. Kang, Y. Shao-Horn, G. Ceder, C.P. Grey, Effect of High Voltage on the Structure and Electrochemistry of $LiNi_{0.5}Mn_{0.5}O_2$: A Joint Experimental and Theoretical Study, Chem. Mater. 18 (2006) 4768–4781. https://doi.org/10.1021/cm060886r.
[19] Y.-K. Sun, D.-J. Lee, Y.J. Lee, Z. Chen, S.-T. Myung, Cobalt-Free Nickel Rich Layered Oxide Cathodes for Lithium-Ion Batteries, ACS Appl. Mater. Interfaces. 5 (2013) 11434–11440. https://doi.org/10.1021/am403684z.
[20] J.U. Choi, N. Voronina, Y.-K. Sun, S.-T. Myung, Recent Progress and Perspective of Advanced High-Energy Co-Less Ni-Rich Cathodes for Li-Ion Batteries: Yesterday, Today, and Tomorrow, Advanced Energy Materials. 10 (2020) 2002027. https://doi.org/10.1002/aenm.202002027.
[21] J. Zhang, X. Tan, L. Guo, Y. Jiang, S. Liu, H. Wang, X. Kang, W. Chu, Origin of Performance Differences of Nickel-Rich $LiNi_{0.9}Mn_{0.1}O_2$ Cathode Materials Synthesized in Oxygen and Air, Energy Technology. 7 (2019) 1800752. https://doi.org/10.1002/ente.201800752.
[22] J.T. Zhang, X.H. Tan, L.M. Guo, Y. Jiang, S.N. Liu, H.F. Wang, X.H. Kang, W.G. Chu, Controllable formation of lithium carbonate surface phase during synthesis of nickel-rich $LiNi_{0.9}Mn_{0.1}O_2$ in air and its protection role in electrochemical reaction, Journal of Alloys and Compounds. 771 (2019) 42–50. https://doi.org/10.1016/j.jallcom.2018.08.243.
[23] A. Aishova, G.-T. Park, C.S. Yoon, Y.-K. Sun, Cobalt-Free High-Capacity Ni-Rich Layered $Li[Ni_{0.9}Mn_{0.1}]O_2$ Cathode, Advanced Energy Materials. 10 (2020) 1903179. https://doi.org/10.1002/aenm.201903179.
[24] X. Wang, Y.-L. Ding, Y.-P. Deng, Z. Chen, Ni-Rich/Co-Poor Layered Cathode for Automotive Li-Ion Batteries: Promises and Challenges, Advanced Energy Materials. 10 (2020) 1903864. https://doi.org/10.1002/aenm.201903864.
[25] S. Lee, W. Li, A. Dolocan, H. Celio, H. Park, J.H. Warner, A. Manthiram, In-Depth Analysis of the Degradation Mechanisms of High-Nickel, Low/No-Cobalt Layered Oxide Cathodes for Lithium-Ion Batteries, Advanced Energy Materials. 11 (2021) 2100858. https://doi.org/10.1002/aenm.202100858.
[26] J.R. Croy, D.C. O'Hanlon, S. Sharifi-Asl, M. Murphy, A. Mane, C.-W. Lee, S.E. Trask, R. Shahbazian-Yassar, M. Balasubramanian, Insights on the Stabilization of Nickel-Rich Cathode Surfaces: Evidence of Inherent Instabilities in the Presence of Conformal Coatings, Chem. Mater. 31 (2019) 3891–3899. https://doi.org/10.1021/acs.chemmater.8b04332.
[27] W. Zhu, X. Huang, T. Liu, Z. Xie, Y. Wang, K. Tian, L. Bu, H. Wang, L. Gao, J. Zhao, Ultrathin Al2O3 Coating on $LiNi_{0.8}Co_{0.1}Mn_{0.1}O_2$ Cathode Material for Enhanced Cycleability at Extended Voltage Ranges, Coatings. 9 (2019) 92. https://doi.org/10.3390/coatings9020092.
[28] G. Dai, H. Du, S. Wang, J. Cao, M. Yu, Y. Chen, Y. Tang, A. Li, Y. Chen, Improved electrochemical performance of $LiNi_{0.8}Co_{0.15}Al_{0.05}O_2$ with ultrathin and thickness-controlled TiO_2 shell via atomic layer deposition technology, RSC Advances. 6 (2016) 100841–100848. https://doi.org/10.1039/C6RA21903A.
[29] Z.-F. Tang, R. Wu, P.-F. Huang, Q.-S. Wang, C.-H. Chen, Improving the electrochemical performance of Ni-rich cathode material $LiNi_{0.815}Co_{0.15}Al_{0.035}O_2$ by removing the lithium residues and forming Li_3PO_4 coating layer, Journal of Alloys and Compounds. 693 (2017) 1157–1163. https://doi.org/10.1016/j.jallcom.2016.10.099.
[30] T. Deng, X. Fan, L. Cao, J. Chen, S. Hou, X. Ji, L. Chen, S. Li, X. Zhou, E. Hu, D. Su, X.-Q. Yang, C. Wang, Designing In-Situ-Formed Interphases Enables Highly Reversible Cobalt-Free $LiNiO_2$ Cathode for Li-ion and Li-metal Batteries, Joule. 3 (2019) 2550–2564. https://doi.org/10.1016/j.joule.2019.08.004.

Pursuant to the DOE Public Access Plan, this document represents the authors' peer-reviewed, accepted manuscript.
The published version of the article is available from the relevant publisher.

[31] E. Markevich, G. Salitra, Y. Talyosef, U.-H. Kim, H.-H. Ryu, Y.-K. Sun, D. Aurbach, High-Performance $LiNiO_2$ Cathodes with Practical Loading Cycled with Li metal Anodes in Fluoroethylene Carbonate-Based Electrolyte Solution, ACS Appl. Energy Mater. 1 (2018) 2600–2607. https://doi.org/10.1021/acsaem.8b00304.
[32] H. Quang Pham, E.-H. Hwang, Y.-G. Kwon, S.-W. Song, Approaching the maximum capacity of nickel-rich $LiNi_{0.8}Co_{0.1}Mn_{0.1}O_2$ cathodes by charging to high-voltage in a non-flammable electrolyte of propylene carbonate and fluorinated linear carbonates, Chemical Communications. 55 (2019) 1256–1258. https://doi.org/10.1039/C8CC10017A.
[33] W. Xue, M. Huang, Y. Li, Y.G. Zhu, R. Gao, X. Xiao, W. Zhang, S. Li, G. Xu, Y. Yu, P. Li, J. Lopez, D. Yu, Y. Dong, W. Fan, Z. Shi, R. Xiong, C.-J. Sun, I. Hwang, W.-K. Lee, Y. Shao-Horn, J.A. Johnson, J. Li, Ultra-high-voltage Ni-rich layered cathodes in practical Li metal batteries enabled by a sulfonamide-based electrolyte, Nat Energy. 6 (2021) 495–505. https://doi.org/10.1038/s41560-021-00792-y.
[34] A.K. Haridas, Q.A. Nguyen, T. Terlier, R. Blaser, S.L. Biswal, Investigating the Compatibility of TTMSP and FEC Electrolyte Additives for $LiNi_{0.5}Mn_{0.3}Co_{0.2}O_2$ (NMC)–Silicon Lithium-Ion Batteries, ACS Appl. Mater. Interfaces. 13 (2021) 2662–2673. https://doi.org/10.1021/acsami.0c19347.
[35] J. Yang, Q. Liu, K.Z. Pupek, T.L. Dzwiniel, N.L. Dietz Rago, J. Cao, N. Dandu, L. Curtiss, K. Liu, C. Liao, Z. Zhang, Molecular Engineering to Enable High-Voltage Lithium-Ion Battery: From Propylene Carbonate to Trifluoropropylene Carbonate, ACS Energy Lett. 6 (2021) 371–378. https://doi.org/10.1021/acsenergylett.0c02400.
[36] J. Yun, L. Zhang, Q. Qu, H. Liu, X. Zhang, M. Shen, H. Zheng, A Binary Cyclic Carbonates-Based Electrolyte Containing Propylene Carbonate and Trifluoropropylene Carbonate for 5V Lithium-Ion Batteries, Electrochimica Acta. 167 (2015) 151–159. https://doi.org/10.1016/j.electacta.2015.03.159.
[37] Y.-M. Lee, K.-M. Nam, E.-H. Hwang, Y.-G. Kwon, D.-H. Kang, S.-S. Kim, S.-W. Song, Interfacial Origin of Performance Improvement and Fade for 4.6 V $LiNi_{0.5}Co_{0.2}Mn_{0.3}O_2$ Battery Cathodes, J. Phys. Chem. C. 118 (2014) 10631–10639. https://doi.org/10.1021/jp501670g.
[38] M. He, C.-C. Su, C. Peebles, Z. Zhang, The Impact of Different Substituents in Fluorinated Cyclic Carbonates in the Performance of High Voltage Lithium-Ion Battery Electrolyte, J. Electrochem. Soc. 168 (2021) 010505. https://doi.org/10.1149/1945-7111/abd44b.
[39] M. He, C.-C. Su, Z. Feng, L. Zeng, T. Wu, M.J. Bedzyk, P. Fenter, Y. Wang, Z. Zhang, High Voltage $LiNi_{0.5}Mn_{0.3}Co_{0.2}O_2$/Graphite Cell Cycled at 4.6 V with a FEC/HFDEC-Based Electrolyte, Advanced Energy Materials. 7 (2017) 1700109. https://doi.org/10.1002/aenm.201700109.
[40] X. Fan, L. Chen, O. Borodin, X. Ji, J. Chen, S. Hou, T. Deng, J. Zheng, C. Yang, S.-C. Liou, K. Amine, K. Xu, C. Wang, Non-flammable electrolyte enables Li-metal batteries with aggressive cathode chemistries, Nature Nanotech. 13 (2018) 715–722. https://doi.org/10.1038/s41565-018-0183-2.
[41] Z. Zhang, L. Hu, H. Wu, W. Weng, M. Koh, P. C. Redfern, L. A. Curtiss, K. Amine, Fluorinated electrolytes for 5 V lithium-ion battery chemistry, Energy & Environmental Science. 6 (2013) 1806–1810. https://doi.org/10.1039/C3EE24414H.
[42] C. Xu, F. Lindgren, B. Philippe, M. Gorgoi, F. Björefors, K. Edström, T. Gustafsson, Improved Performance of the Silicon Anode for Li-Ion Batteries: Understanding the Surface Modification Mechanism of Fluoroethylene Carbonate as an Effective Electrolyte Additive, Chem. Mater. 27 (2015) 2591–2599. https://doi.org/10.1021/acs.chemmater.5b00339.
[43] J. Liu, L. Zhou, W. Yu, A. Yu, Effect of fluoroethylene carbonate as an electrolyte solvent in the $LiNi_{0.5}Mn_{1.5}O_4$/$Li_4Ti_5O_{12}$ cell, Journal of Alloys and Compounds. 812 (2020) 152064. https://doi.org/10.1016/j.jallcom.2019.152064.

Pursuant to the DOE Public Access Plan, this document represents the authors' peer-reviewed, accepted manuscript.
The published version of the article is available from the relevant publisher.

[44] Y.-B. He, F. Ning, B. Li, Q.-S. Song, W. Lv, H. Du, D. Zhai, F. Su, Q.-H. Yang, F. Kang, Carbon coating to suppress the reduction decomposition of electrolyte on the $Li_4Ti_5O_{12}$ electrode, Journal of Power Sources. 202 (2012) 253–261. https://doi.org/10.1016/j.jpowsour.2011.11.037.
[45] C. Han, Y.-B. He, H. Li, B. Li, H. Du, X. Qin, F. Kang, Suppression of interfacial reactions between $Li_4Ti_5O_{12}$ electrode and electrolyte solution via zinc oxide coating, Electrochimica Acta. 157 (2015) 266–273. https://doi.org/10.1016/j.electacta.2014.12.080.
[46] M.C. López, G.F. Ortiz, J.R. González, R. Alcántara, J.L. Tirado, Improving the Performance of Titania Nanotube Battery Materials by Surface Modification with Lithium Phosphate, ACS Appl. Mater. Interfaces. 6 (2014) 5669–5678. https://doi.org/10.1021/am500189h.
[47] G.F. Ortiz, M. Cabello, M.C. López, J.L. Tirado, M.J. McDonald, Y. Yang, Exploring a Li-ion battery using surface modified titania nanotubes versus high voltage cathode nanowires, Journal of Power Sources. 303 (2016) 194–202. https://doi.org/10.1016/j.jpowsour.2015.10.104.
[48] G.F. Ortiz, M.C. López, Y. Li, M.J. McDonald, M. Cabello, J.L. Tirado, Y. Yang, Enhancing the energy density of safer Li-ion batteries by combining high-voltage lithium cobalt fluorophosphate cathodes and nanostructured titania anodes, Sci Rep. 6 (2016) 20656. https://doi.org/10.1038/srep20656.
[49] M. Cabello, G.F. Ortiz, M.C. López, P. Lavela, R. Alcántara, J.L. Tirado, Self-assembled $Li_4Ti_5O_{12}/TiO_2/Li_3PO_4$ for integrated Li–ion microbatteries, Electrochemistry Communications. 56 (2015) 61–64. https://doi.org/10.1016/j.elecom.2015.04.011.
[50] S. Rubio, R. Ruiz, W. Zuo, Y. Li, Z. Liang, D. Cosano, J. Gao, Y. Yang, G.F. Ortiz, Insights into the Reaction Mechanisms of Nongraphitic High-Surface Porous Carbons for Application in Na- and Mg-Ion Batteries, ACS Appl. Mater. Interfaces. 14 (2022) 43127–43140. https://doi.org/10.1021/acsami.2c09237.
[51] L. Xing, W. Li, C. Wang, F. Gu, M. Xu, C. Tan, J. Yi, Theoretical Investigations on Oxidative Stability of Solvents and Oxidative Decomposition Mechanism of Ethylene Carbonate for Lithium Ion Battery Use, J. Phys. Chem. B. 113 (2009) 16596–16602. https://doi.org/10.1021/jp9074064.
[52] M.C. Biesinger, B.P. Payne, B.R. Hart, A.P. Grosvenor, N.S. McIntryre, L.W. Lau, R.S. Smart, Quantitative chemical state XPS analysis of first row transition metals, oxides and hydroxides, J. Phys.: Conf. Ser. 100 (2008) 012025. https://doi.org/10.1088/1742-6596/100/1/012025.
[53] G. Assat, D. Foix, C. Delacourt, A. Iadecola, R. Dedryvère, J.-M. Tarascon, Fundamental interplay between anionic/cationic redox governing the kinetics and thermodynamics of lithium-rich cathodes, Nat Commun. 8 (2017) 2219. https://doi.org/10.1038/s41467-017-02291-9.
[54] C. Wang, Y.S. Meng, K. Xu, Perspective—Fluorinating Interphases, J. Electrochem. Soc. 166 (2018) A5184. https://doi.org/10.1149/2.0281903jes.
[55] K. Tasaki, A. Goldberg, J.-J. Lian, M. Walker, A. Timmons, S.J. Harris, Solubility of Lithium Salts Formed on the Lithium-Ion Battery Negative Electrode Surface in Organic Solvents, J. Electrochem. Soc. 156 (2009) A1019. https://doi.org/10.1149/1.3239850.
[56] S.K. Heiskanen, J. Kim, B.L. Lucht, Generation and Evolution of the Solid Electrolyte Interphase of Lithium-Ion Batteries, Joule. 3 (2019) 2322–2333. https://doi.org/10.1016/j.joule.2019.08.018.
[57] J.E. Owejan, J.P. Owejan, S.C. DeCaluwe, J.A. Dura, Solid Electrolyte Interphase in Li-Ion Batteries: Evolving Structures Measured In situ by Neutron Reflectometry, Chem. Mater. 24 (2012) 2133–2140. https://doi.org/10.1021/cm3006887.
[58] J. Yan, B.-J. Xia, Y.-C. Su, X.-Z. Zhou, J. Zhang, X.-G. Zhang, Phenomenologically modeling the formation and evolution of the solid electrolyte interface on the graphite

Pursuant to the DOE Public Access Plan, this document represents the authors' peer-reviewed, accepted manuscript.
The published version of the article is available from the relevant publisher.

electrode for lithium-ion batteries, Electrochimica Acta. 53 (2008) 7069–7078. https://doi.org/10.1016/j.electacta.2008.05.032.
[59] N. Schulz, R. Hausbrand, C. Wittich, L. Dimesso, W. Jaegermann, XPS-Surface Analysis of SEI Layers on Li-Ion Cathodes: Part II. SEI-Composition and Formation inside Composite Electrodes, J. Electrochem. Soc. 165 (2018) A833. https://doi.org/10.1149/2.0881803jes.
[60] Y. Yu, P. Karayaylali, Y. Katayama, L. Giordano, M. Gauthier, F. Maglia, R. Jung, I. Lund, Y. Shao-Horn, Coupled $LiPF_6$ Decomposition and Carbonate Dehydrogenation Enhanced by Highly Covalent Metal Oxides in High-Energy Li-Ion Batteries, J. Phys. Chem. C. 122 (2018) 27368–27382. https://doi.org/10.1021/acs.jpcc.8b07848.
[61] C.L. Campion, W. Li, B.L. Lucht, Thermal Decomposition of $LiPF_6$-Based Electrolytes for Lithium-Ion Batteries, J. Electrochem. Soc. 152 (2005) A2327. https://doi.org/10.1149/1.2083267.
[62] N. Schulz, R. Hausbrand, L. Dimesso, W. Jaegermann, XPS-Surface Analysis of SEI Layers on Li-Ion Cathodes: Part I. Investigation of Initial Surface Chemistry, J. Electrochem. Soc. 165 (2018) A819. https://doi.org/10.1149/2.0061805jes.
[63] S.K. Heiskanen, J. Kim, B.L. Lucht, Generation and Evolution of the Solid Electrolyte Interphase of Lithium-Ion Batteries, Joule. 3 (2019) 2322–2333. https://doi.org/10.1016/j.joule.2019.08.018.
[64] L. Yang, B. Ravdel, B.L. Lucht, Electrolyte Reactions with the Surface of High Voltage LiNi0.5Mn1.5O4 Cathodes for Lithium-Ion Batteries, Electrochem. Solid-State Lett. 13 (2010) A95. https://doi.org/10.1149/1.3428515.
[65] Y. Li, Y. Li, A. Pei, K. Yan, Y. Sun, C.-L. Wu, L.-M. Joubert, R. Chin, A.L. Koh, Y. Yu, J. Perrino, B. Butz, S. Chu, Y. Cui, Atomic structure of sensitive battery materials and interfaces revealed by cryo–electron microscopy, Science. 358 (2017) 506–510. https://doi.org/10.1126/science.aam6014.
[66] K.N. Wood, G. Teeter, XPS on Li-Battery-Related Compounds: Analysis of Inorganic SEI Phases and a Methodology for Charge Correction, ACS Appl. Energy Mater. 1 (2018) 4493–4504. https://doi.org/10.1021/acsaem.8b00406.

Pursuant to the DOE Public Access Plan, this document represents the authors' peer-reviewed, accepted manuscript. The published version of the article is available from the relevant publisher.